Climate Dynamics (2025) 63:146
https://doi.org/10.1007/s00382-025-07626-7

ORIGINAL ARTICLE

Spatio-temporal evolution of compound hot and dry extremes synchronizations in Europe

Domenico Giaquinto[1,2] · **Giorgia Di Capua**[3] · **Warner Marzocchi**[1,4] · **Jürgen Kurths**[1,2,5]

Received: 4 September 2024 / Accepted: 4 February 2025

Abstract
The probability of incidence of compound extreme climate events is increasing due to human-induced climate change: in particular, there is high confidence that concurrent hot and dry extremes will become more frequent with increased global warming. In this context, Europe is no exception. Understanding the aggregated impact of synchronized compound hot and dry events at different locations is a pressing issue, especially when it comes to predicting these extremes. We use concepts and methods derived from network theory to highlight hotspot regions in Europe where these spatially compound extremes are increasing and analyse the atmospheric precursors driving these anomalous conditions. Using ERA5 reanalysis data and focusing on the summer and winter seasons of the period 1941-2020, we construct evolving networks constituted by 51 consecutive blocks, encoding the spatial synchronization structure of compound hot and dry events. Next, we highlight the regional and seasonal differences of compounds occurrences and synchronizations, unraveling the main changes in the graphs structure, identifying hotspot regions and, finally, describing the atmospheric conditions behind compound events. The increase of compounds frequency and spatial synchronizations do not always match: synchronizations increase in South-eastern Europe during winter and in some locations in Finland, north of Poland and the Baltic states in summer, although, in both cases, we do not detect a corresponding trend in compounds occurrences. Moreover, we show that most of the synchronizations evolution can be explained by atmospheric pressure dynamical changes, including NAO and SNAO intensity. This work brings out key aspects concerning the underlying spatio-temporal dynamics of concurrent hot and dry events.

Keywords Compound extreme climate events · Spatially compound hot and dry extremes · Evolving complex networks · Climate networks · Climate change

1 Introduction

Global warming sets new unprecedented temperature records every year, with 2023 identified as the hottest year on record (Copernicus Climate Change Service 2024c) and June 2024 being the thirteenth warmest month in a row compared to the respective months in the past (Copernicus Climate Change Service 2024f). As a direct consequence, the increase in intensity and duration of climate and weather extremes poses serious societal and environmental threats, such as biodiversity loss (Habibullah et al. 2022), water scarcity for most of the population (Zhang et al. 2019), impacts on human health and mortality (Yadav et al. 2023). These events have been reported by several studies over the last

✉ Warner Marzocchi
warner.marzocchi@unina.it

Domenico Giaquinto
domenico.giaquinto@unina.it

Giorgia Di Capua
dicapua@pik-potsdam.de

Jürgen Kurths
Juergen.Kurths@pik-potsdam.de

[1] Modeling and Engineering Risk and Complexity, Scuola Superiore Meridionale, Naples 80138, Italy

[2] Complexity Science, Potsdam Institute for Climate Impact Research (PIK) - Member of the Leibniz Association, Potsdam 14473, Germany

[3] Earth System Analysis, Potsdam Institute for Climate Impact Research (PIK) - Member of the Leibniz Association, Potsdam 14473, Germany

[4] Dipartimento di Scienze della Terra, dell'Ambiente e delle Risorse, University of Naples "Federico II", Naples 80138, Italy

[5] Department of Physics, Humboldt University, Berlin 10117, Germany

Published online: 05 March 2025

decades (AghaKouchak et al. 2020; Fischer et al. 2021; Seneviratne et al. 2021), with the aim of understanding and predicting future occurrences to reduce risk and implement adaptation strategies. Still, many scientific challenges lay ahead.

Single extremes located in distant regions could be statistically related, due to numerous and often nonlinear mechanisms. In such circumstances, the superposition principle does not hold, and when multiple events hit, the associated impacts are larger than the sum of the single ones (Zscheischler et al. 2018). These phenomena are referred to as *climate and weather compound events* (Zscheischler et al. 2020), which have been the topic of several recent research papers. Climate compound events have been classified into different types (Zscheischler et al. 2020), e.g., (i) spatially compounding climate events, where multiple locations are affected by climate hazards within a short time window, or also (ii) temporally compounding events, in case of a temporal sequence of extremes at one location. Whereas about the specific involved hazards, several examples have been brought to the attention in the literature: hot-humid (Li et al. 2020) or hot-dry (Ha et al. 2022; Tian et al. 2024) extremes, extreme precipitation and storm surge (Bevacqua et al. 2019), wet-windy (Leeding et al. 2023) and hot-windy (Tavakol et al. 2020) extremes. Thereby, compound events research calls for an interdisciplinary approach, owing to the different processes involved at various spatial and temporal scales, as well as to the implications for society at different levels (Tabari and Willems 2023).

Europe has been reported as one of the major heatwaves hot-spots in the northern hemisphere, also due to the persistence of double jet states over Eurasia (Rousi et al. 2022). Here, heatwaves have been the most impactful climate hazard in terms of human fatalities (Douris and Kim 2021), e.g., in summer 2003 (Di Napoli et al. 2018; Fink et al. 2004), when more than 70,000 deaths were caused by strong temperatures (Robine et al. 2008), or the more recent 2022 heatwave (Ballester et al. 2023), which induced water shortages and wildfires across large parts of western and southern Europe (Tripathy and Mishra 2023). Concerning dry extremes (Spinoni et al. 2015b), several studies agree that while the north of the continent is experiencing wetter than average conditions, the Mediterranean has seen more severe and frequent drought states (Spinoni et al. 2017; Copernicus Climate Change Service 2024g). This is mainly due to the increased precipitation over northern latitudes, and the simultaneous temperature increase and precipitation decrease over the Mediterranean (Spinoni et al. 2015a). The occurrence of both extreme flooding and droughts with high spatial variability has been confirmed by the European State of the Climate 2023 (Copernicus Climate Change Service 2024b). The persistence of precipitation deficiency is a warning signal for the development of other types of droughts too, such as agricultural droughts (Wilhite and Glantz 1985; Seneviratne et al. 2012). For instance, just consider the high correlation between 2023 precipitation (Copernicus Climate Change Service 2024a) and soil moisture (Copernicus Climate Change Service 2024e) anomaly in Europe. River discharge is also affected by low precipitation, like in the case of the Po River, which experienced below-average flow throughout the entire year (Copernicus Climate Change Service 2024d).

As for compound hot and dry extremes, it has become evident that these events will become more frequent and severe due to global warming across large areas of Earth (Seneviratne et al. 2021; Tian et al. 2024). Potential feedback mechanisms linking these two conditions further exacerbate the risk (Seneviratne et al. 2021, 2010). For instance, temperatures in high-latitude regions may be critically influenced by the snow-albedo feedback (Hall and Qu 2006), while soil moisture-temperature feedback (Seo and Ha 2022) are thought to contribute to the additional warming observed over mid-latitude land areas compared to the global mean temperature increase (Vogel et al. 2017; Seneviratne et al. 2018). Using a climate model ensemble, Lorenz et al. (2016) show the influence of soil moisture variability on the intensity, frequency, and duration of temperature extremes, as well as its connection to precipitation extremes. Both atmospheric processes and land surface mechanisms contribute to the observed negative temperature-precipitation correlation (Berg et al. 2015).

Simultaneous hot and dry extremes impact the European continent in multiple ways, affecting primary production (Ciais et al. 2005; Zscheischler et al. 2017), increasing wildfire risk (Gudmundsson et al. 2014; Ruffault et al. 2016; Sutanto et al. 2020), and raising mortality rates (Stott et al. 2004; Ionita et al. 2017). Several studies agree that the rise in compound hot and dry extremes in Europe is primarily driven by atmospheric conditions (Tian et al. 2024; Manning et al. 2019; De Luca and Donat 2023). Rising temperatures promote the transition from meteorological drought to soil moisture depletion by enhancing evapotranspiration (Manning et al. 2019), especially in wetter regions (Manning et al. 2018). In these areas, reduced precipitation, commonly linked to decreased cloud cover and anticyclonic circulation patterns, leads to higher net radiation, which increases evapotranspiration and water scarcity in the soil (Teuling et al. 2013). Higher temperatures further intensify this process, particularly in northern and central Europe, where rainfall levels have not significantly declined (De Luca and Donat 2023). However, this mechanism is limited in drier regions where soil moisture is already low. This is particularly true for western Europe and the Mediterranean, where both decreasing precipitation and rising temperatures contribute to extreme compound hot and dry conditions (Zhao et al. 2024).

Nonetheless, regardless of the specific mechanisms involved, it is clear that the frequency of hot and dry extremes across Europe is generally increasing. However, little has been done to assess whether co-occurring hot and dry extremes in different locations-i.e., spatially compound hot and dry extremes (SCHADEs)-are also on the rise. Assessing the trends and atmospheric conditions driving simultaneous compound hot and dry events across multiple locations is essential to improve the predictability of these extremes and to implement tailored adaptation strategies in hotspot regions. Previous studies associated spatially compound extremes to amplified planetary waves (Kornhuber et al. 2020), modes of climate variability (De Luca et al. 2020) or large-scale variability patterns (Ye and Messori 2020).

Here, we aim to assess if and how the synchronizations of SCHADE events are changing in Europe. Complex networks represent a promising tool in this perspective. Various real-world systems such as power grids (Arianos et al. 2009), the internet (Maslov et al. 2004), human contacts (Goh et al. 2007), and more (Ausloos et al. 2017; Bardoscia et al. 2021), can be conceptualized as the result of the interactions of many dynamical units, whose relationships structure often encodes and influences the system dynamics (Boccaletti et al. 2006). Over the past two decades, the climate system has been approached through network theory as well, complementing the well–established methodologies of physical modeling (Tsonis and Roebber 2004; Ying et al. 2020). Under this framework, climate is approximated via a grid of low dimensional nonlinear dynamical units (Donges et al. 2009b). In this study, we employ spatially embedded climate networks, whose nodes are constituted by geographical sites on a regular latitude-longitude grid, while the links are established based on the degree of statistical similarity between processes occurring at different locations. Once the network structure is established, its topology is studied to get new insights into the statistical relationships and/or spatial patterns of the analyzed phenomena. Spatially embedded climate networks have been used to describe numerous climate processes at different spatio-temporal scales (Boers et al. 2019; Gupta et al. 2021; Giaquinto et al. 2023), and to study climate extremes (Vallejo-Bernal et al. 2023; Ludescher et al. 2021). Using ERA5 reanalysis data (Hersbach et al. 2023), we model the European SCHADEs synchronization structure as an evolving climate complex network, constructing one evolving network for boreal summer (June, July and August) and one for boreal winter (December, January and February) of the period 1941–2020. This approach allows us to describe synchronization trends at the local and regional scales, highlighting hot-spot regions for synchronized compounds and connecting the graph structure to atmospheric circulation patterns.

The remainder of the paper is organized as follows: in Sect. 2 we describe the data and the methodology we adopt in this study; in Sect. 3 we present the results; Sect. 4 is dedicated to the discussion, and conclusions are drawn in Sect. 5.

2 Data and methods

2.1 Spatial domain and data

In this study we focus on hot and dry extremes on European land grid points, defined as the territory between 30° and 72.6° N latitude and −10° and 40° E longitude. This area results from the merging of the IPCC Sixth Assessment Report regions North Europe (NEU), West and Central Europe (WCE) and Mediterranean (MED) (Iturbide et al. 2020); the latter is further subdivided in East (EMed) and West Mediterranean (WMed), as reported in Fig. 1. Since we define dry states based on precipitation regimes, desert locations (according to the Köppen-Geiger climate classification, see Peel et al. (2007)) are excluded, given their low rainfall levels (Fig. 1).

We use ERA5 reanalysis data (Hersbach et al. 2023) for 1941–2020 summer (June, July and August, JJA) and the winter (December, January and February, DJF) seasons (leap days are removed). We employ the daily maximum temperature at 2 m (T_{max}) [°C], the daily cumulated precipitation (P) [m] and the geopotential height at 500 hPa ($Z500$) [m]. For each of these fields, we estimate the trend from the best-fit line using least-squares at each time step and remove it, assuming it linear in a first-order approximation. T_{max} and P are collected with $0.25° \times 0.25°$ spatial resolution for the land area shown in Fig. 1, while $Z500$ is collected at $1° \times$

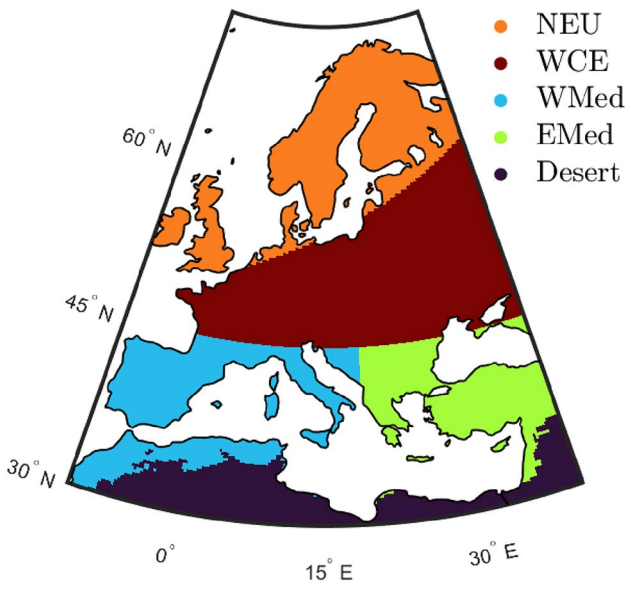

Fig. 1 Spatial domain and subregions used in this study. Desert and sea locations are not considered in our work

1° resolution for the entire globe. We also employ mean sea level pressure data (*SLP*) [Pa] at $1° \times 1°$ resolution to compute daily North Atlantic Oscillation (NAO) and Summer NAO (SNAO) indices for the winter and summer seasons, respectively (for more details, please see the Supplementary Material, Text S1).

2.2 Definition of hot, dry and compound extremes

The 1941–1970 period is used as reference to determine the historical distributions of maximum temperatures and cumulated precipitation for each location i of our spatial domain, i.e., grid points on the regular $0.25° \times 0.25°$ European lattice (19,425 nodes in total). This period is used as a reference following the climate normals convention (World Meteorological Organization 2017), i.e., the use of a 30–years baseline condition to assess climate states at a given location.

A hot extreme occurs at grid point i on day d if the following is satisfied:

$$T_{\max}(i,d) \geq \{(T_{\max}(i,[d-15,d+15]))_{[1941,1970]}\}_{90th}, \quad (1)$$

i.e., the maximum temperature of d and of the 15 days which precede and follow d are collected for the 1941–1970 reference period; this results in $31 * 30 = 930$ values, which constitute the historical distribution of maximum daily temperature of day d and location i; the 90th percentile of this set is used as threshold (right hand-side of Eq. 1) to identify hot extremes. Similarly, a dry extreme is detected at location i on day d if:

$$\sum_{t=d-30}^{d} P(i,t) \leq \left\{ \left(\sum_{t=d-30}^{d} P(i,t) \right)_{[1941,1970]} \right\}_{10th}, \quad (2)$$

i.e., the observed cumulated precipitation during the last 31 days including d is lower or equal than the 10th percentile of the historical distribution. In this case, since we use cumulated precipitation, this historical distribution is constituted by 30 values. Each calendar day is thus assigned to a specific threshold to define the hot and dry extreme occurrences respectively. Since our data are detrended, we also account for the higher temperature baseline of recent times compared to the past. Our results are thus based on detrended anomalies and both the climatological and seasonal cycles are removed (Di Capua et al. 2020). Since our definition of extremes is percentile-based, stationary time series should have the same number of single hot (dry) extremes. However, although we remove the linear trend from the data prior to identify the extremes, we do not observe a uniform spatial distribution of single extremes (see Figure S2). This is due to the non-stationary variance of the temporal series: even if the trend is removed from the mean, a trend in the extreme values of the distribution still remains for some nodes.

Finally, for each location i, a compound event is detected on day d if both a hot and a dry extremes occur. This way, we get binary event series of compound events for each location i for the entire analysed period 1941–2020.

2.3 Network construction via event synchronization

The SCHADEs network is established following the climate network reconstruction from data approach described by Fan et al. (2021) and applied in several studies in the recent past (Boers et al. 2019; Vallejo-Bernal et al. 2023; Gupta et al. 2021; Ludescher et al. 2021). Given the event-like time series of compound events, we use Event Synchronization (ES) (Quian Quiroga et al. 2002; Malik et al. 2012) as statistical similarity measure to estimate the compounds concurrences between each pair of nodes. ES is particularly suited for our purposes because it is designed to treat event-like time series. It has been extensively used to construct climate extreme events networks, proving to be enough efficient and informative (Giaquinto et al. 2023; Malik et al. 2010; Agarwal et al. 2017; Strnad et al. 2023). The degree of synchronicity among nodes i, j is measured based on the number of quasi–simultaneous events occurrences between the associated event series. Event l occurring at i at time t_l^i is considered to be synchronized with event m occurring at j at time t_m^j if $|t_l^i - t_m^j| < \tau_{lm}^{ij}$, where

$$\tau_{lm}^{ij} = min\{|t_{l+1}^i - t_l^i|, |t_l^i - t_{l-1}^i|, |t_{m+1}^j - t_m^j|, |t_m^j - t_{m-1}^j|, t_{\max}\}/2. \quad (3)$$

Since the time lag τ_{lm}^{ij} is specific to each event pairs and it is dynamically computed, there is no need to set it a priori (Quian Quiroga et al. 2002). By setting $t_{\max} = 14$ we ensure that only concurrences developing in a time window of maximum 7 days are counted as synchronizations. This maximum lag is chosen considering that hot extremes are usually detected on timescales of at least three days (Russo et al. 2015; Perkins and Alexander 2013), while precipitation deficiency could last for several months (Spinoni et al. 2014). Therefore, the duration of compound hot and dry events, the way we define it, is limited by the temperature anomaly and it is restricted to few days.

A score J_{lm}^{ij} is assigned to every events pair l and m according to the following rule:

$$J_{lm}^{ij} = \begin{cases} 1, & \text{if } |t_l^i - t_m^j| < \tau_{lm}^{ij} \\ 0, & \text{otherwise} \end{cases}. \quad (4)$$

Next, the number of times an event at i is synchronized with an event at j is counted:

$$C(i,j) = \sum_{l=1}^{S_i} \sum_{m=1}^{S_j} J_{lm}^{ij}, \quad (5)$$

where S_i and S_j are the total number of events in i and j, respectively. C is then normalized to get the synchronization score Q:

$$Q(i,j) = \frac{C(i,j)}{\sqrt{S_i S_j}}. \tag{6}$$

We use the undirected version of ES ($Q(i,j) = Q(j,i)$), since we are not concerned with the direction of synchronicity; therefore, the resulting network is undirected.

The significance of the synchronization scores $Q(i,j)$ is tested via surrogate data. Similar approaches to null model construction have been used in previous climate networks studies (Boers et al. 2019; Vallejo-Bernal et al. 2023; Rheinwalt et al. 2016). For each node pair i and j, we construct 500 surrogate series of j by uniformly and randomly shuffling block of events year–wise; afterwards, we calculate the null model distribution of $Q(i,j)$ by performing ES for the 500 i and j pairs. By uniformly and randomly redistributing year-blocks rather than events, any seasonal serial correlation is preserved, which is assumed to be meaningless across seasons. We test the sensitivity of our results to a higher number of surrogates (up to 2000), finding no major variations.

For each observed $Q(i,j)$, we compute its associated p-value using the respective null model. The p-values are corrected using the Benjamini-Hochberg false discovery rate approach (Benjamini and Hochberg 1995; Benjamini and Yekutieli 2001) to account for multiple significance testing (we perform $\simeq 10^8$ comparisons). Finally, a link between nodes i and j is defined if $Q(i,j)$ is significant at $\alpha = 0.01$. Different choices of significance levels for link attribution are possible (Boers et al. 2019; Gupta et al. 2021; Vallejo-Bernal et al. 2023; Ludescher et al. 2021), leading to different network densities. We choose $\alpha = 0.01$ to limit the density of the network, but keeping enough links to get informative results. The resulting network is undirected and unweighted. Since the links model the significant synchronizations shared between nodes, we use the terms link and significant synchronization, or more simply synchronization, interchangeably.

2.4 The evolving network approach

We employ an evolving networks framework (Fig. 2) to analyse the temporal evolution of SCHADEs synchronizations patterns in JJA and DJF separately.

The 1941–2020 period is divided in 51 blocks using a 30–year time window, moving with a one year step. For each of the 51 30–year time windows, one network block is established using the procedure described in Sect. 2.3. While the nodes are fixed (the 19,425 grid points on the regular 0.25° × 0.25° European lattice), the links depend on the different SCHADEs synchronizations taking place during each 30–year block.

2.5 Network indices

Numerous network measures can be used to assess the properties of a graph (Boccaletti et al. 2006), several of which have been applied in climate networks studies (Donges et al. 2009b), e.g., local measures like the degree centrality (Gupta et al. 2021), mesoscale measures like the clustering coefficient (Gupta et al. 2021), global measures like the closeness (Donges et al. 2009a) and the betweenness centrality (Boers et al. 2013), or even community detection algorithms (Giaquinto et al. 2023). In this study, we employ the regional and cross-regional link densities (ρ), the degree centrality (DC) and the clustering coefficient (CC) to get insights into the main features of the evolving networks.

The regional link density ρ_S of region S is defined as the ratio between the total number of links connected to nodes belonging to region S, $e(S)$, and the maximum possible number of links that could be connected to nodes of region S, $e(S)_{\max}$, also including intra–connections of region S:

$$\rho_S = \frac{e(S)}{e(S)_{\max}}. \tag{7}$$

The cross-regional link density $\rho_{S,T}$ between regions S and T is defined as the ratio between the total number of links

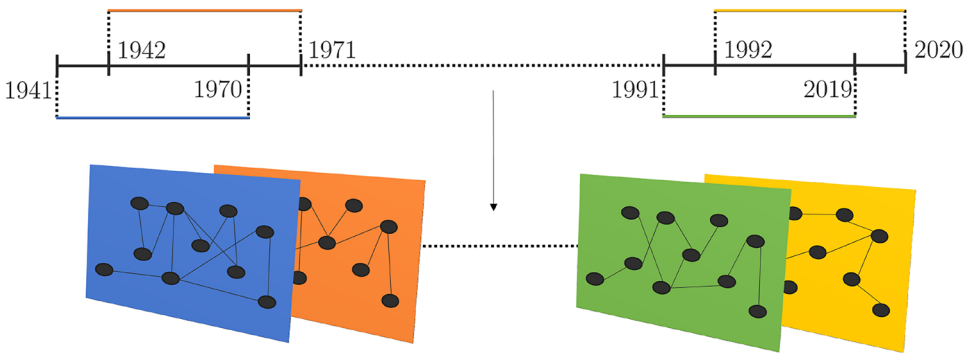

Fig. 2 General framework to construct the evolving network. The entire time period is divided in intervals of 30 years using a time window moving with a one year step, obtaining a total of 51 intervals. For each of the 51 30–year intervals, one different network block is built for the analysed European land area. This procedure is separately carried for the JJA and DJF seasons

connecting region S and T, $e(S, T)$, and the maximum possible number of links that could connect S and T, $e(S,T)_{\max}$:

$$\rho_{S,T} = \frac{e(S,T)}{e(S,T)_{\max}}. \tag{8}$$

Both densities are normalized and range between 0 and 1. This is necessary for comparing regions of different sizes, as larger regions are likely to have more links than smaller ones.

The DC_v of node v is expressed as

$$DC_v = \sum_{i=1}^{N} a(v,i), \tag{9}$$

where N is the total number of nodes in the network and $a(v, i)$ is the entry of the adjacency matrix A, which equals 1 if nodes v and i are connected, and 0 otherwise. The DC is the number of links attached to a given node, i.e., the number of neighbors of the node, and thus represent the significant synchronizations the specific grid point has with the rest of the graph. Nodes with higher degree are characterized by more connections, and, since a link is attributed when a significant synchronization between two locations is detected, nodes with higher degree have more synchronizations.

The CC measures the degree to which nodes tend to cluster, i.e., to form closed triangles with their neighbors:

$$CC_v = \frac{e(\Gamma_v)}{\frac{DC_v(DC_v-1)}{2}}, \tag{10}$$

where $e(\Gamma_v)$ is the number of existing edges in Γ_v, which is the set of neighbors of node v, and $\frac{(DC_v(DC_v-1))}{2}$ is the maximum number of possible edges in Γ_v. The CC lies between 0 and 1, with $CC_v = 1$ meaning that v and its neighbors form a clique, and $CC_v = 0$ meaning that v neighbors are not connected, i.e., v is the center of a star graph with its neighbors.

The spatial patterns displayed by network measures depend on the artificial boundaries introduced when setting the domain of the study. These boundaries cut the links that would connect the considered grid points with locations not included in the present work. This cause the emergence of boundary effects on the spatial patterns of network measures which need to be corrected (Rheinwalt et al. 2012). For every block of the two evolving networks, we construct 1000 spatially embedded random networks (SERNs) surrogates by assigning links based on the probability of observing a link of the same length in the original graph. Afterwards, the boundary effects for the DC and the CC are estimated by averaging that specific measure over the SERNs, node–wise. The corrected measure is obtained by dividing the original index by the corresponding average one of the SERN surrogates. The final corrected measure represents the value of the network index relative to the expected value from the spatial embedding, and thus it is dimensionless.

We assess the evolution of the network indices by looking at their trend across the 51 network blocks, node–wise. Since the blocks are constructed from overlapping time windows (Fig. 2), independence can not be assumed. Therefore, we apply the sieve bootstrap method (Kreiss 1997; Bühlmann 1997) to test the significance of the detected trends. The data are filtered using an auto–regressive (AR) process whose order is estimated via the Akaike information criterion from the original data; next, the residuals are repeatedly resampled to be used as generating noise of the previously estimated AR process. This way, bootstrapped time series are obtained, which have a temporal structure similar to the original data and can be used to perform a statistical test of choice. In our case, for each node we simulate 1000 bootstrapped series of DC and CC, which we use to perform a standard t-test to assess the significance of the observed trends (Noguchi et al. 2011).

2.6 Geopotential height composites

To analyze the atmospheric conditions corresponding to the occurrence of compound hot and dry extremes, we use Z500 composites during high compound days (HCD), i.e., the top 10% of days ranked based on the total number of compound events occurrences for each of the regions depicted in Fig. 1. For instance, the Z500 JJA composite of NEU for the period 1941–1970 is computed as follows: among the 2,760 JJA days (92 days × 30 years), we extract the 276 days for which the number of NEU compound events is highest; the composite is then obtained by averaging Z500 over these selected HCD. Besides, when the composite is derived for two regions, the set of days is the one resulting from the intersection of the HCD of the two regions. For instance, the Z500 JJA composite of NEU&WCE for the period 1941–1970 is computed as follows: the 276 NEU HCD and the 276 WCE HCD are intersected to identify the time steps used to compute the Z500 field average. If the two HCD sets are independent, the time steps should be ~27, i.e., 1% of the initial 2,760 JJA days.

3 Results

3.1 Spatial distribution of compound hot and dry extremes

Figure 3a–b shows the distribution of compound extremes for JJA and DJF. Summer shows a higher number of compound extremes compared to winter, especially in the center and in the north of the continent: most locations record 200 events (i.e., an average of 2.5 extremes per

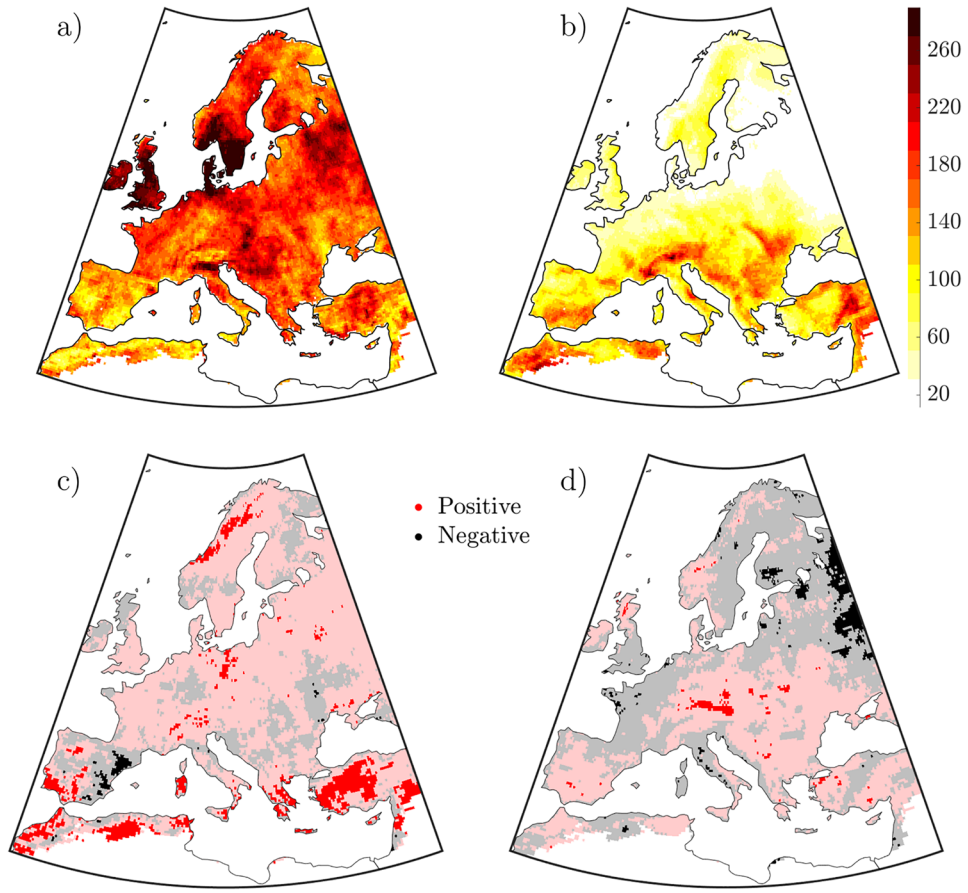

Fig. 3 Spatial distribution and trend of compound events. Number of compound events during 1941 - 2020 for **a** the JJA season and **b** the DJF season. Seasonal trend of compound events for **c** the JJA season and **d** the DJF season. The fully opaque colour represent a significant trend with $\alpha = 0.05$, while the lighter, semi-transparent colour denotes a non-significant trend

season) or more, with peaks exceeding 260 occurrences. During winter, only a few nodes reach 200 events, primarily in the Mediterranean, while the rest shows fewer than 100 events. Great Britain and southern Scandinavia are major hotspots in JJA, followed by the Po valley, the Hungarian plain and western Russia. During DJF, northern and central Europe are less affected by compound extremes, while the Mediterranean region experiences higher occurrences. In terms of annual trends (Fig. 3c–d), most of the significant increasing trends are detected in the Mediterranean in JJA (with the notable exception of eastern Spain), while a few locations display a compound increase in DJF, with significant negative trends in western Russia and in some locations in northwestern France, England, Finland and Italy. Since temperature and precipitation time series are detrended (see Sect. 2.1), these trends are related to compound events themselves and not to temperature or precipitation increase/decrease. Compound trends p-values are shown in Figure S1, while the spatial distribution of hot and dry extremes separately are shown in Figure S2.

3.2 Evolution of significant synchronizations

Figure 4 exhibits the evolution of the regional link density (the ratio between the number of links connected to the region and the maximum possible number of links that could be connected to the region) and the cross-regional one (the ratio between the number of links connecting two regions and the maximum possible number of links that could connect them) in the 51 JJA and DJF evolving networks blocks.

The regional density rises during summer in the second part of the analysed period, in particular for NEU and WCE (Fig. 4a). For these two regions, the density is higher and more rapidly increasing ($\rho_{NEU}, \rho_{WCE} \approx <$ *spanclass* $='$ *convertEndash*$' > 0.1-0.15 <$ */span* $>$) compared to the Mediterranean ($\rho_{EMed}, \rho_{WMed} \approx 0.05$). During winter (Fig. 4b), the Mediterranean density is higher, as expected from Fig. 3b, and it is comparable to the WCE one, while NEU shows a decreasing density

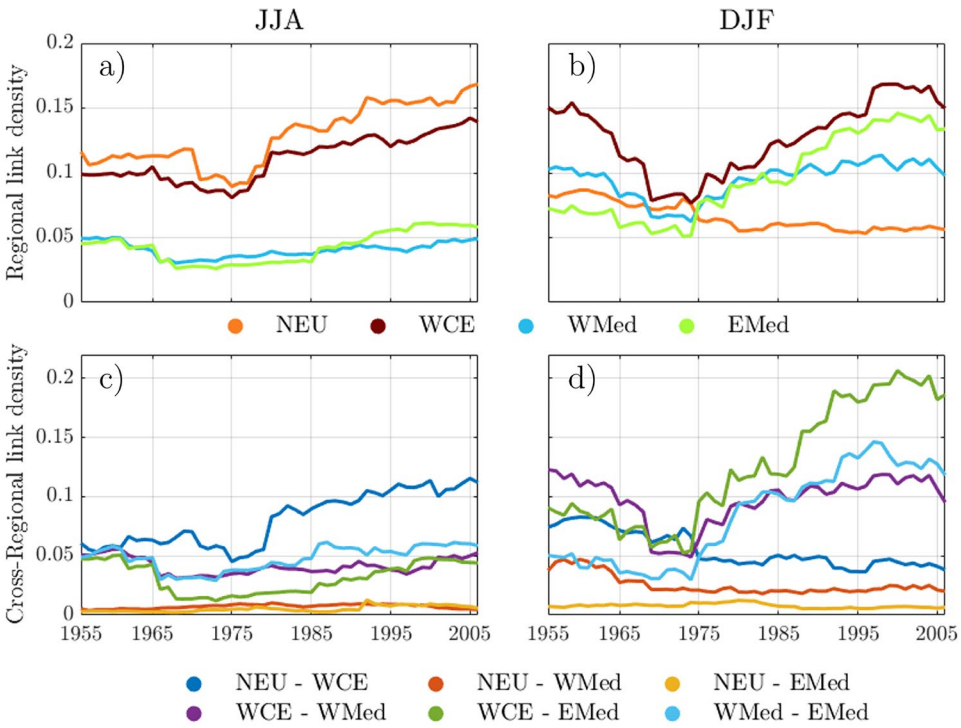

Fig. 4 Evolution of link density. Regional density of the 51 evolving networks blocks for the **a** JJA and **b** DJF season. Cross-regional density of the 51 evolving networks blocks for the **c** JJA and **d** DJF season. The central year of each network block is used as reference on the x-axis

($\rho_{NEU} \approx <$ *spanclass* $=' convertEndash' > 0.08 - 0.05 <$ */span* $>$), being the only region with a clear negative evolution of significant synchronizations.

During summer (Fig. 4c), NEU is strongly connected to WCE with increasing cross-regional density ($\rho_{NEU,WCE} \approx <$ *spanclass* $=' convertEndash' > 0.05 - 0.1 <$ */span* $>$), but it shares few synchronizations with the Mediterranean ($\rho_{NEU,WMed}, \rho_{NEU,EMed} \lessapprox 0.01$). WCE maintains a rather stable connection with both WMed and EMed ($\rho_{WCE,WMed}, \rho_{WCE,EMed} \approx 0.05$), which are also well tied together ($\rho_{WMed,EMed} \approx 0.05$); in this latter case, after an initial drop, the cross-regional density increases after 1975. During winter (Fig. 4d), the cross-regional densities change substantially. WCE and the Mediterranean remain coupled but with more links compared to summer ($\rho_{WCE,WMed} \approx 0.1$) and a stronger increasing trend in the case of WCE-EMed ($\rho_{WCE,EMed} \approx <$ *spanclass* $=' convertEndash' > 0.1 - 0.2 <$ */span* $>$). WMed and EMed also show a stronger connection and increasing trend during DJF compared to JJA ($\rho_{WMed,EMed} \approx <$ *spanclass* $=' convertEndash' > 0.05 - 0.15 <$ */span* $>$). Conversely, NEU is isolating from the rest of the continent: the NEU-WCE connections decrease and the NEU-EMed and NEU-WMed bonds remain low.

These observations are in line with the spatial distributions in Fig. 3a–b: the higher link density of central and northern Europe matches their elevated number of compounds in JJA, while the few occurrences of NEU hot and dry compounds in DJF is reflected in its small and decreasing density.

3.3 Evolution of degree centrality

The average DC and its evolution across the 51 network blocks in JJA and DJF is shown in Figs. 5 and 6, respectively. During summer, northern Europe is characterized by the highest number of synchronizations: here, the average degree reaches peak values of 2, while it is ≈1 elsewhere (Fig. 5a). This partly confirms what observed in compound events spatial distribution (Fig. 3a): a higher number of events results in higher average DC, i.e., more link density and thus significant synchronizations occurrences. Indeed, NEU regional link density is the highest in JJA, reaching values above 0.15 (Fig. 4a). As for the average DC in DJF, most of the Mediterranean, central–western Europe and Great Britain stand out (Fig. 5b). Some parallelisms with the events distribution are possible (Fig. 3b): for instance, the high number of events in eastern Turkey and the corresponding large degree (DC $\approx <$ *spanclass* $=' convertEndash' > 1.4 - 2 <$ */span* $>$), or similarly the higher number of events and DC in alpine and Apennines regions (DC ≈ 2) compared to the Po valley (DC ≈ 1.2). In the case of Great Britain, northern France and Germany, the comparison between number of events and average DC is less trivial: here, the DC appears to be relatively high (Fig. 5b) even if few compounds occurrences are formed (Fig. 3b). Indeed, spatial synchronizations and

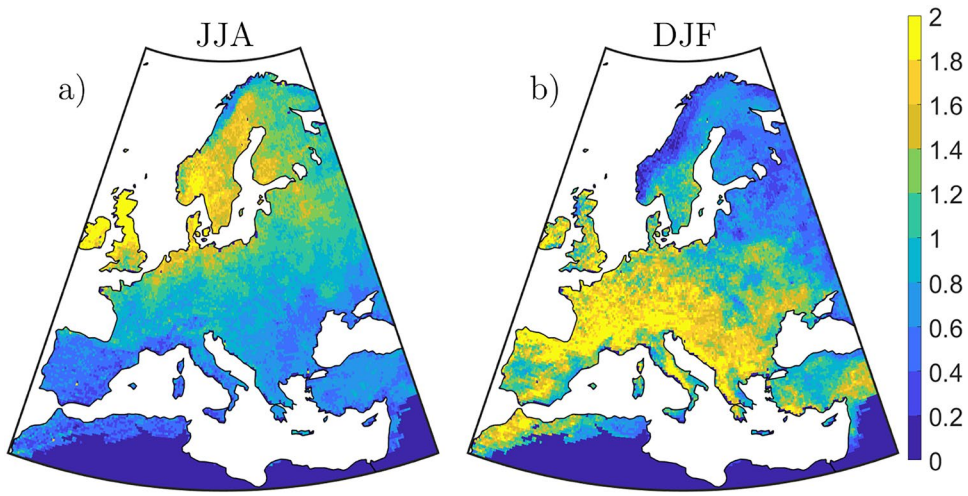

Fig. 5 Average degree centrality. Average value of DC across the 51 network blocks for **a** JJA and **b** DJF. The DC is dimensionless because of the correction of bias due to spatial embedding

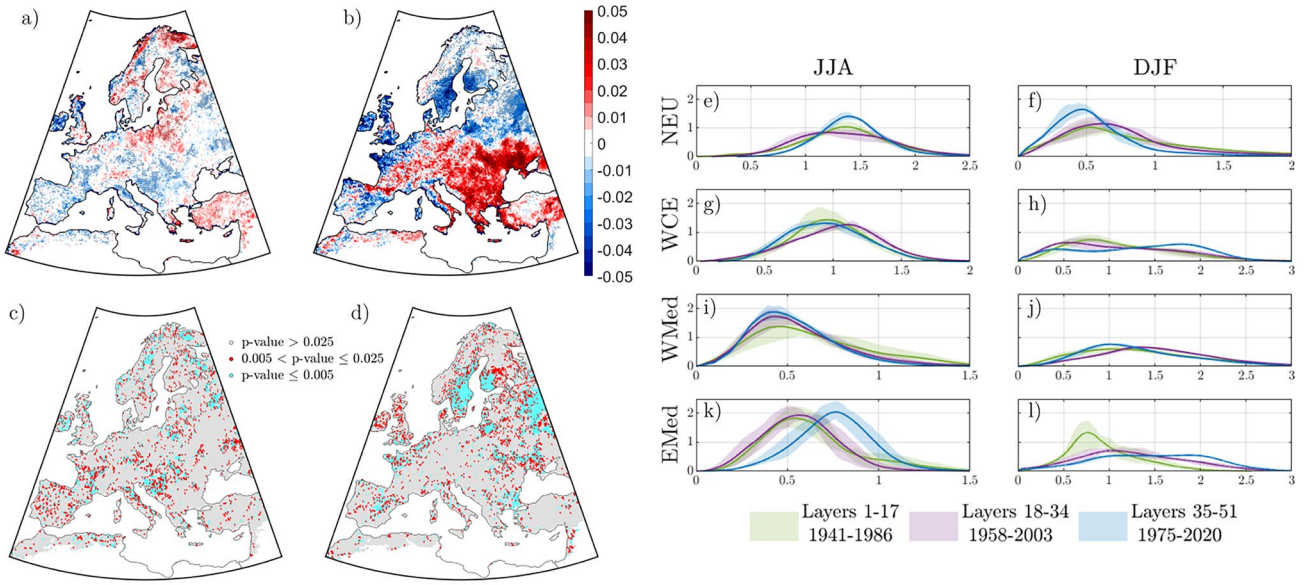

Fig. 6 Evolution of degree centrality. DC trend for **a** JJA and **b** DJF. Dots are drawn if the trend is significant at $\alpha = 0.05$ (two-sided sieve bootstrap t-test). *p*-values of the detected DC trends for **c** the JJA season and **d** the DJF season. **e–l** Pdfs (empirically estimated via Gaussian-Kernel distributions) of the degree centrality for JJA and DJF and for every European region. The 51 distributions are divided in 3 groups for which we show the average value (solid lines) and 1 s.t.d. confidence bound (shades). The DC is dimensionless because of the correction of bias due to spatial embedding

number of events do not always match. Few events with high synchronicity or numerous events with low synchronicity can be expected, as shown in more details in the Supplementary Material (Text S2). The higher DJF DC in WCE and the Mediterranean (Fig. 5b) aligns with their relatively high link densities (Fig. 4b).

Figure 6a–b shows the DC trend for each node across the 51 network blocks. An increasing DC (positive trend value in Fig. 6a–b) means a growing number of significant synchronizations for the specific node; conversely, a decreasing DC (negative trend value in Fig. 6a–b) is indicative of a reduction of synchronizations for the analysed node. While the regional and cross-regional link densities (Fig. 4) give regional information about synchronizations variations, DC trends are useful to make local assessments. Among the locations characterized by an increasing DC trend during JJA (Fig. 6a), those located in Finland, northern Poland and the Baltic states stand out (with increases of DC between 2 and 4%), since in these cases we do not detect a trend in compounds occurrences (Fig. 3c). Similarly, some areas display an increasing number of compound (Fig. 3c), which is not followed

by increasing synchronizations (Fig. 6a), such as in the case of southern Portugal, southern Spain and Northwest Africa. During winter, the differences between compound events and synchronizations evolution is more pronounced: if on the one hand the negative trend of events in western Russia (Fig. 3d) is reflected by the decreasing DC in the same region (with decreases between 1 and 2%, Fig. 6b), on the other hand the DC strongly increases in central southern Europe (with increases up to 5%, Fig. 6b). Finally, the isolation of NEU in DJF suggested from Fig. 4d is confirmed by the significant negative DC trend (up to −5%, Fig. 6b). In panels 6c-d we show the *p*-values of the detected trends. We also analyze the evolution of the DC via empirical distributions (Fig. 6e–l) for JJA and DJF and for the European regions separately. The EMed distributions are shifting towards higher values of DC both in summer and winter (Fig. 6k–l). A negative shift is visible in the case of the WMed region during JJA and DJF (Fig. 6i–j), although not substantial in the latter case. The WCE distribution remains stable in JJA (Fig. 6g), while it tends to become bimodal in the last period of DJF (Fig. 6h): indeed, as we can also see in Fig. 6b, there are WCE nodes with both a significant negative trend (mainly in the northern part of the region) and significant positive trend (in the southeastern part). Finally, in the case of NEU, the DC distribution shifts towards higher values in summer (Fig. 6e), while the shift is opposite in winter (Fig. 6f).

Similar results on the evolution of the clustering coefficient index are shown in the Supplementary Material (Figure S5 and S6), where we see a higher CC during DJF for the entire continent compared to JJA, suggesting a denser and more interconnected synchronizations structure during winter.

3.4 Synchronizations and atmospheric conditions

Here we assess the atmospheric conditions during hot and dry compound events by linking Z500 fields composites to the network structure for each European region.

First, we focus on the summer period for NEU and WCE, since these experience most of the events during JJA (see Fig. 3a). In Fig. 7a–d, we present the Z500 composites during HCD—the top 10% of days for number of compound events occurrences—in the first 30 years of our study period, namely 1941–1970, for NEU (Fig. 7a) and for NEU together with the other regions (Fig. 7b–d); Fig. 7e shows the number of links directed to NEU found in the 1941–1970 network

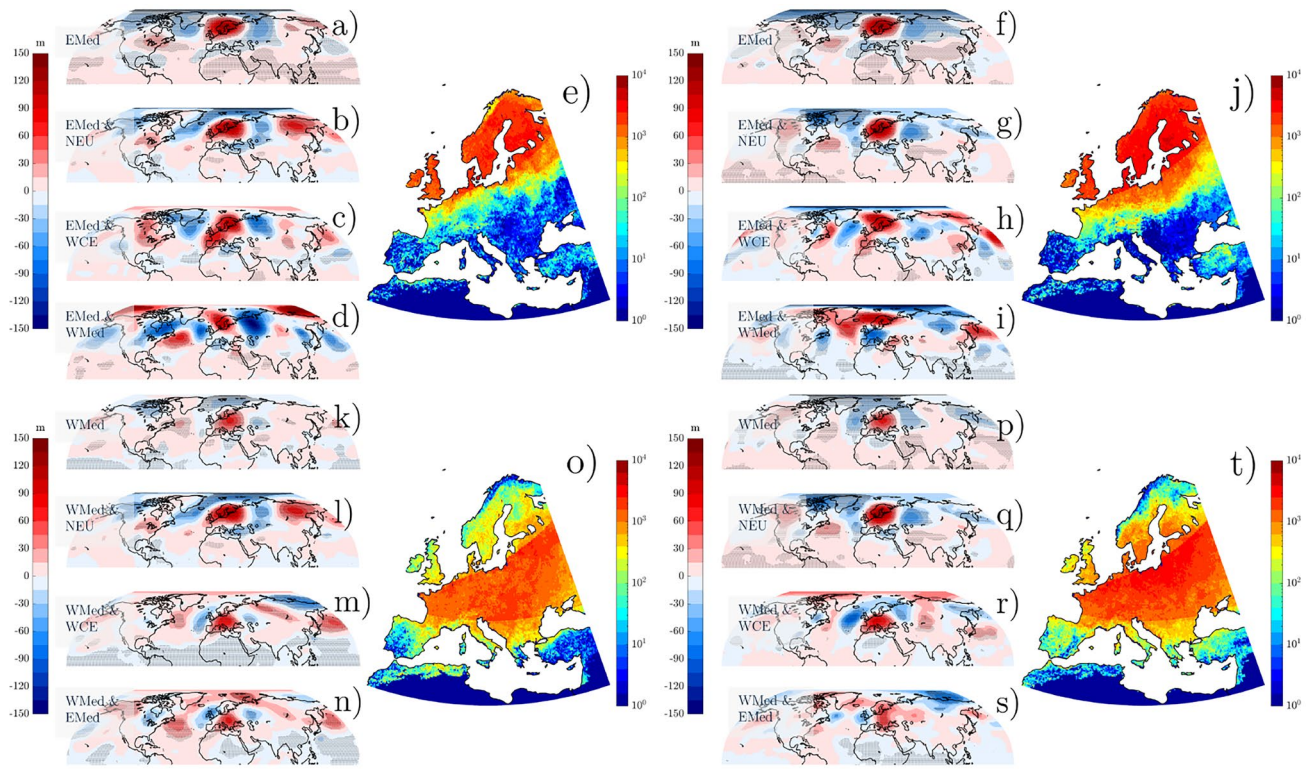

Fig. 7 Geopotential height composites and links variations during JJA. **a–d** Z500 composites during HCD for the indicated regions and for the period 1941–1970. **e** Number of links directed to NEU found in the 1941–1970 network block for each node. **f–j)** Same as panels (**a–e**), but considering the last 30 years of the analysed period, i.e., 1991–2020. **k–t)** Same as panels **(a–j)** but with respect to WCE. For all the composites, black dots are drawn if the Z500 anomaly is significant at $\alpha = 0.05$

block for each node in Europe. For the 1941–1970 NEU composite (Fig. 7a), the Z500 field shows a significant positive anomaly over NEU, with ridges over eastern Canada and northeastern Russia, while negative anomalies lies over northern Canada, Greenland, North Atlantic and western Russia. In the NEU&WCE composite (Fig. 7b), the positive anomaly over Europe shifts southwards and the previously described high pressure systems intensify, while the negative anomalies over northern America, Greenland and western Russia reduce (Fig. 7b), with a trough appearing over Eastern Mediterranean as well. The NEU&WMed composite (Fig. 7c) displays a bigger European ridge, which extends southwards to western Mediterranean, while negative pressure is still present on eastern Mediterranean; high pressure over western North America and negative pressure over Greenland and western Russia still exist. In the case of NEU&EMed (Fig. 7d), ridges are located over Scandinavia and northeastern Asia; low pressure is detected over North Pacific, central US, eastern Canada and western Russia. A significant high-low dipole is located over the North Atlantic. Most of NEU synchronizations are shared with WCE (Fig. 7e); indeed, the corresponding high pressure located over these two areas is significantly high (Fig. 7a–b). Not many links connect NEU with WMed and EMed: while in the case of eastern Europe this is reflected in the composite structure, where the high pressure over NEU is not coupled with a significant pressure over EMed (Fig. 7d), in the case of NEU&WMed the high pressure, albeit present (Fig. 7c), does not cause a large number of synchronizations between NEU and WMed (Fig. 7e).

The 1991–2020 composites (Fig. 7f–i) show interesting differences in comparison to the 1941–1970 ones (Fig. 7a–d). While the composites related to events occurred in NEU are quite similar (Fig. 7a, f), in the NEU&WCE ones the positive anomaly over Europe is stronger in 1991–2020 by approximately +20 m, and it is coupled to a +40 m higher pressure in the North Atlantic, as well as a more distinct lower pressure over Greenland (around −70 m compared to the initial period, Fig. 7b,g). Moreover, while during 1941–1970 compound events in NEU and WCE come with low pressure over Northwest America and high pressure over Northeast Asia, in 1991–2020 the opposite happens (Fig. 7b,g). As for the NEU&WMed composites, the ridge over WMed weakens (Fig. 7c,h). The NEU&EMed composite shows a stronger positive anomaly over high latitudes (up to +100 m compared to 1941–1970) coupled with a more pronounced low pressure over western Europe (about −70 m compared to 1941–1970), and a stronger positive anomaly over Turkey (+20 m, Fig. 7d,i). The synchronizations patterns in Fig. 7j reflect the changes of Z500 fields: NEU and WCE share more connections, synchronizations between NEU and WMed decrease, the connections between Turkey and NEU increase and those between the Balkans and NEU decrease. Overall, these atmospheric patterns confirm what outlined in Fig. 4c: NEU becomes more strongly coupled to WCE in recent times and less connected to the Mediterranean area.

The WCE composite of the period 1941–1970 (Fig. 7k) show positive pressure anomalies over central–eastern Europe, North Atlantic and North Pacific, and low-pressure systems over the Arctic Sea and northern Canada. The WCE&WMed and WCE&EMed composites (Fig. 7m–n) share key structure similarities, i.e., the positive anomaly over central and southern Europe, a positive anomaly over western North Atlantic and a negative one over eastern North Atlantic, the positive anomaly over North Pacific and the negative one over western Russia. Some differences are the negative pressure over northern eastern Asia in the WCE&WMed composite and the positive–negative dipole over North America in the case of the WCE&EMed composite. Panels 7l and b, corresponding to the NEU&WCE composites, are the same.

Regarding the 1991–2020 WCE composites (Fig. 7p–s), their structure is similar to 1941–1970 (Fig. 7k–n), with slightly stronger positive anomalies over central Europe during the last 30 years (about +30 m higher). Nevertheless, a northeastern Atlantic low-Europe high pattern seems to more prominently emerge (Fig. 7p–r) compared to 1941–1970 (Fig. 7k–m). The network structure (Fig. 7o,t) is characterized by a general increase of WCE connections during the last 30 years compared to the past, which is in line with the 1991–2020 stronger positive anomalies. The Z500 composites and links variations for EMed and WMed during JJA are shown in the Supplementary Material (Figure S7).

Concerning the winter period, we show the results for EMed and WMed, as these appear to be the most severely affected by compound occurrences in DJF (Fig. 3b) and the regions with a stronger increasing synchronizations trends in this period (Figs. 4d and 6b). Figure 8a–d shows the Z500 composites for the period 1941–1970 for EMed (Figs. 8a) and for EMed together with the other regions (Fig. 8b–d). The patterns are quite similar, with few differences concerning the precise location of ridges and troughs, which do not change the overall structure: high pressure is located over central–southern Europe, North Atlantic, northeastern North America and North Pacific; low pressure is detected over high latitudes in Europe, Greenland and northeastern Asia. Regarding the EMed&NEU composite, the low-high north–south pressure dipole remains, with high anomalies confined in central-southern Europe, reaching Great Britain and Denmark at most. This separation between the South and the North of the continent is reflected in the EMed links structure shown in Fig. 8e, where we see few connections between NEU and EMed.

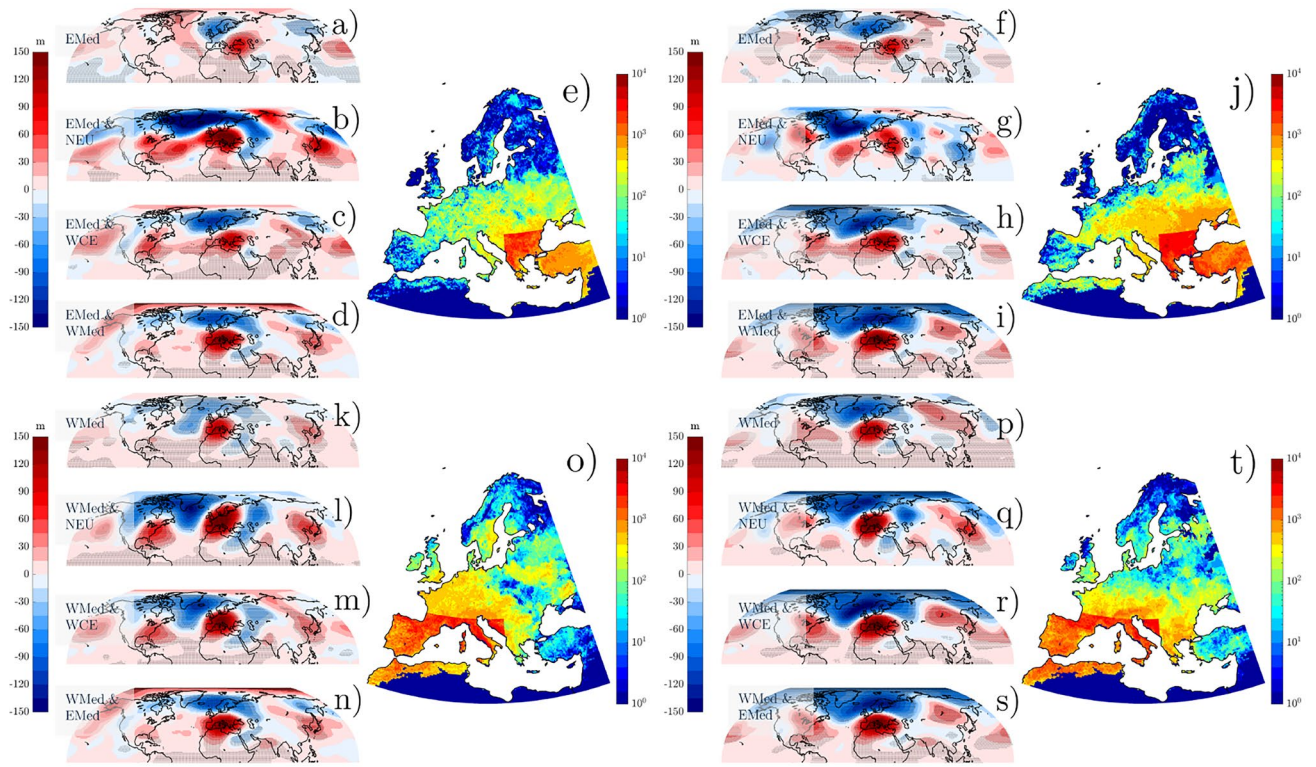

Fig. 8 Geopotential height composites and links variations during DJF. a–d Z500 composites during HCD for the indicated regions and for the period 1941–1970. **e** Number of links directed to EMed found in the 1941–1970 network block for each node. **f–j)** Same as panels (a–e), but considering the last 30 years of the analysed period, i.e., 1991–2020. **k–t** Same as panels (a–j) but with respect to WMed. For all the composites, black dots are drawn if the Z500 anomaly is significant at $\alpha = 0.05$

During 1991–2020, the EMed composites (Fig. 8f–i) are similar to those related to 1941–1970 (Fig. 8a–d), but the low-high north–south dipole located over Europe and the Atlantic is more pronounced, except for NEU&EMed (Fig. 8b,g). The 1991–2020 connections (Fig. 8j) are higher compared to the initial period (Fig. 8e), except for those between NEU and EMed.

The 1941–1970 WMed composites (Fig. 8k–n) and 1991–2020 (Fig. 8p–s) show similar features to the EMed ones (Fig. 8a–d,f–i), with high pressure over southern Europe shifted towards the West. We also observe high pressure systems over northeastern America, eastern Russia and North Pacific, while troughs are located over northern Canada, Greenland and western Russia. The major difference between the initial and the last period is the enhanced low-high north–south dipole located over Europe and the North Atlantic during 1991–2020. In recent times (Fig. 8t), WMed appears to share more links with EMed and southern WCE, and less with NEU and northern WCE with respect to 1941–1970 (Fig. 8o). Thus, the spatial synchronizations of both EMed and WMed increase in the south and decrease with northern regions; this is accompanied by a strengthened negative pressure in northern Europe and North Atlantic and positive pressure over central and southern Europe. The Z500 composites and links variations for NEU and WCE during DJF are shown in the Supplementary Material (Figure S8).

3.5 Temperature and precipitation conditions during high compound days

Changes in compound synchronizations structure due to large scale atmospheric patterns are most likely related to the impact of pressure anomaly on temperature and precipitation due to land-atmosphere feedbacks. The increase and/or decrease of temperature and precipitation intensity drive the occurrence of compound hot and dry events. Thus, we analyze temperature and precipitation anomalies during HCD for each studied region. Specifically, we conduct this analysis for compound events in NEU and WCE during JJA, and for compound events in WMed and EMed during DJF. We connect atmospheric regimes to compound events intensity in two ways: (i) examining changes in temperature and precipitation distributions during HCD

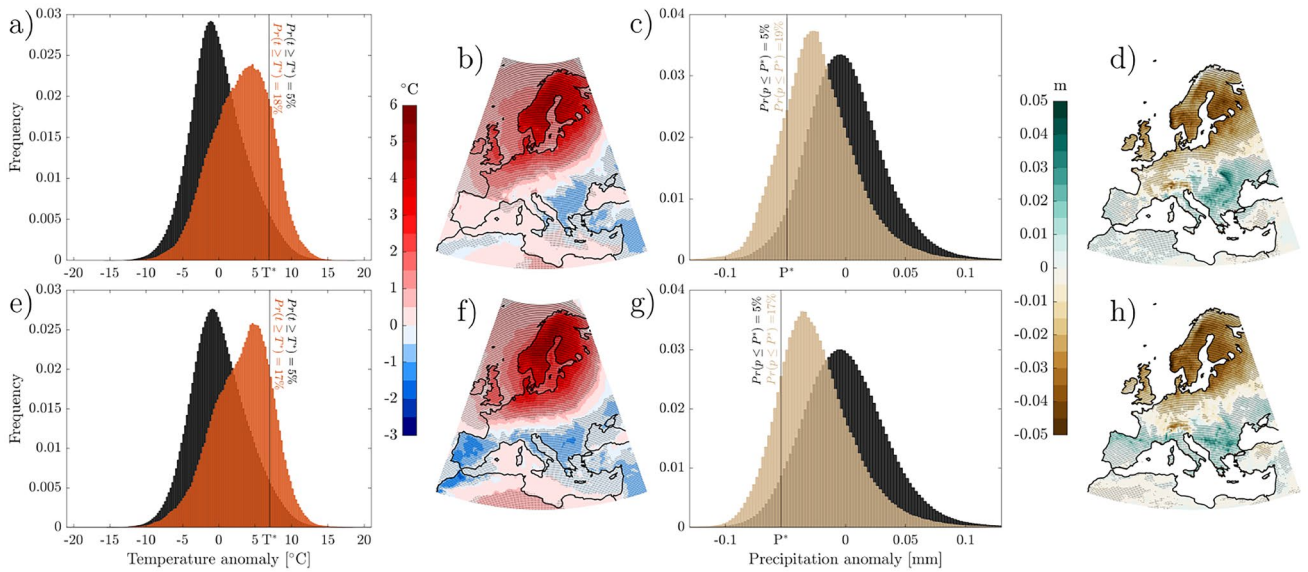

Fig. 9 Temperature and precipitation anomalies for NEU in JJA. **a,c** Histogram plots of temperature (**a**) and precipitation (**b**) for the JJA season in 1941–1970 (black histograms) and for HCD (temperature in red and precipitation in brown). The black line indicates the 95th (5th) percentile T^* (P^*) of the complete JJA temperature (precipitation) distribution. The probability of exceeding this temperature (precipitation) level during HCD is shown in red (brown). The number of elements in each bin is normalized with the to the total number of elements. **b,d** Temperature (**b**) and precipitation (**d**) composites during HCD. Black dots are drawn if the anomaly is significant at $\alpha = 0.05$. **e,h** Same as (**a–d**) but for 1991–2020

compared to the entire JJA or DJF season, and (ii) analyzing temperature and precipitation composites during HCD, so to get a spatial information of temperature and precipitation changes. The analysis is conducted for both 1941–1970 and 1991–2020, following the approach used to derive Figs. 7 and 8.

In Fig. 9, we focus on temperature and precipitation anomalies in JJA for the NEU region.

In 1941–1971 (top panels), NEU temperature anomalies during HCD (Fig. 9a, red histograms) are shifted towards higher values compared to all JJA seasons (black histograms). The 95th percentile of the temperature anomaly across all JJA seasons, T^*, is exceeded by definition 5% of the time. However, during HCD, the exceedance frequency of T^* increases to 18%, more than a 3-fold increase. This is reflected in the temperature composite shown in Fig. 9b, where temperatures are substantially higher (up to +6°C) over NEU and northern WCE, while significant low values are observed over EMed (down to −1°C). Precipitation is lower during HCD, with the probability of falling below the 5th percentile of the full period, P^*, reaching up to 19%, i.e., almost a 4-fold increase. (Fig. 9c). The precipitation composite indicates dry conditions over NEU (Fig. 9d), particularly in southern Norway, Sweden, and southern Finland, as well as in parts of the Alpine region, with values down to −0.05 m of cumulated precipitation per month. Conversely, significantly high precipitation is observed over EMed (up to +0.05 m of cumulated precipitation per month in Ukraine).

In 1991–2020 (Fig. 9, bottom panels), both temperature and precipitation anomalies over NEU exhibit more extreme conditions compared to 1941–1970. Probabilities of exceeding T^* and falling below P^* remain elevated (Fig. 9e,g), with more than a 3-fold increase for both. The temperature anomaly is higher (Fig. 9f) compared to 1941–1970 (Fig. 9b), with most of Scandinavia having temperature anomalies over +5°C. Differently from 1941–1970, western Mediterranean is characterized by cooler conditions, up to −1.5°C. Precipitation decreases over NEU during 1991–2020 (Fig. 9h) compared to 1941–1970 (Fig. 9d), with more locations in Scandinavia down to −0.05 m of cumulated precipitation per month. Hence, it exists a direct connection between the intensifying high-pressure systems shown in Fig. 7a,f and the intensity of extremes during HCD (Fig. 9). Large-scale atmospheric circulation patterns can drive the occurrence of both hot and dry extremes (Ionita et al. 2021), with high-pressure systems often leading to elevated temperatures and reduced precipitation (Kautz et al. 2022), as we also discuss in more details in Sect. 4. This connection is further reflected in the structure of NEU compound synchronizations: during more recent times, NEU shows stronger coupling with WCE and weaker connections to the Mediterranean area, consistent with the changes in temperature and precipitation composites depicted in

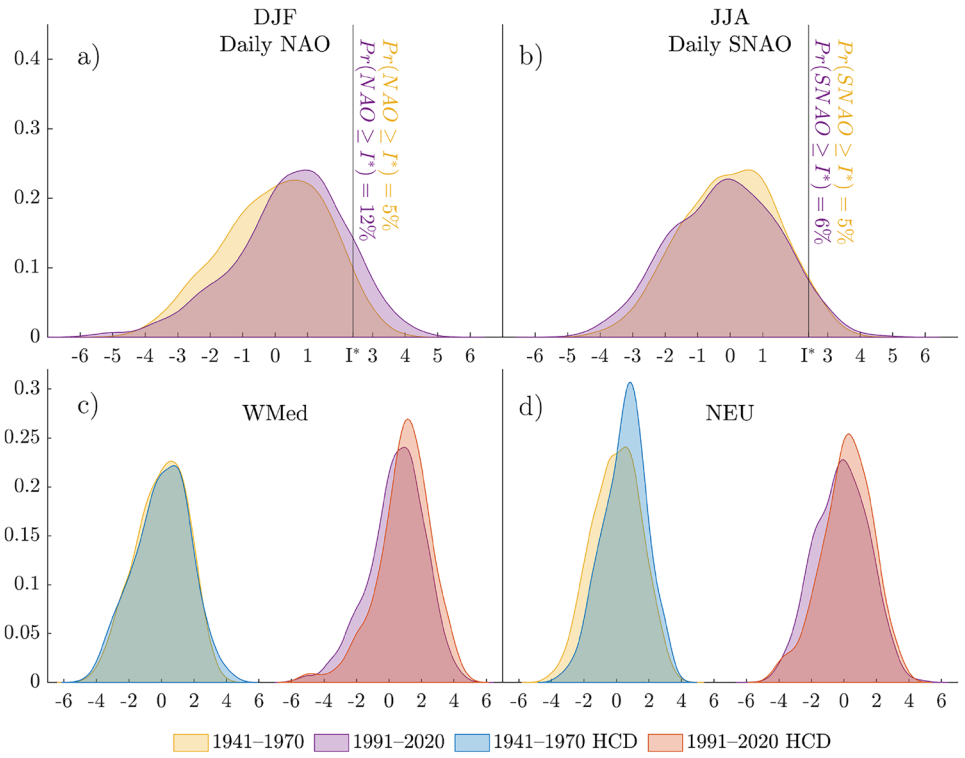

Fig. 10 The evolution of daily NAO and SNAO indices and their relation with high compound days. **a** Daily NAO intensity evolution in DJF between 1941–1970 (yellow distribution) and 1991–2020 (violet). **b** Same as (**a**) but for the SNAO daily index in JJA. **c** Comparison between daily DJF NAO intensity during 1941–1970 (yellow) and daily DJF NAO intensity during WMed HCD in 1941–1970 (blue) and analogously for 1991–2020 (violet) and WMed HCD in 1991–2020 (red). **d** Same as (**c**) but for JJA SNAO and NEU

Fig. 9b,f and d,h. Similar results are found for the other regions, WCE in JJA and WMed and EMed in DJF (see Supplementary Material, Figures S9-11), which shows strong connections between Z500 composites, temperature and precipitation intensities, and network structure.

3.6 NAO and SNAO patterns during high compound days

We check the relationship between NAO intensity and compound occurrences during DJF in WMed and EMed, as well as between SNAO intensity and compound occurrences during JJA in NEU and WCE. The intensity of the daily NAO index in DJF increases during 1991–2020 compared to 1941–1970 (Fig. 10a), with probability of exceeding the 95th percentile of the initial period, I^*, more than double, reaching up to 12%. Conversely, the daily SNAO index during JJA does not sensibly change (Fig. 10b).

When comparing the NAO intensity in 1941–1970 with the one during WMed HCD in the same period, we notice minor differences (Fig. 10c), with the median of both distribution ≈ 0.12. Conversely, in 1991–2020, this difference raises, with increase of NAO+ conditions: while the median of NAO intensity in 1991–2020 is ≈ 0.62, it reaches ≈ 1.05 during WMed HCD (Fig. 10c). A similar scenario holds true in the case of EMed (see Supplementary Material, Figure S12c). Figure 10d shows the SNAO intensity during NEU HCD, both in the case of 1941–1970 and 1991–2020. During HCD, the daily SNAO is more likely to be in a positive phase for both periods. The median of the entire period shifts from ≈ 0.05 to ≈ 0.60 during NEU HCD in 1941–1970, and from ≈ -0.10 to ≈ 0.23 during NEU HCD in 1991–2020. In the case of WCE HCD, we do not find considerable differences between SNAO average intensity and SNAO intensity during HCD (see Supplementary Material, Figure S12d).

We also explore the prevalence of HCD during months with high NAO/SNAO intensity. The results partly confirm what shown by Fig. 10 and S12: WMed and EMed HCD are more prevalent in months with stronger NAO in 1991–2020 (Figure S13); this is less evident for NEU HCD and months with high SNAO intensity, while no differences are found for WCE HCD (Figure S14).

4 Discussion

Europe is one of the major heatwave hotspot in the Northern Hemisphere (Kornhuber et al. 2019; Mitchell et al. 2019; Robine et al. 2008; Ballester et al. 2023). However, understanding the evolution of wet and dry conditions due to global warming is a challenge, due to the high spatio-temporal variability of extreme precipitation and droughts in Europe (Copernicus Climate Change Service 2024b). Thermodynamic mechanisms are not enough to explain dynamical changes, such as anomalous circulation patterns,

which play a key role in this context (Coumou et al. 2014; Di Capua et al. 2021; White et al. 2022).

Large-scale atmospheric patterns can act as dynamic drivers of hot and dry conditions. High-pressure systems are typically associated with subsidence and clear-sky conditions. This has a two–fold effect: (i) the incoming solar radiation increases, resulting in higher surface temperatures (Tian et al. 2023), and (ii) precipitation reduces due to decreased cloud cover. Under these conditions, the land–atmosphere coupling (Lesk et al. 2021) – the negative correlation between temperature and precipitation – is intensified, also due to the role of soil moisture (Berg et al. 2015). The lack of precipitation caused by clear skies reduces soil moisture (Seneviratne et al. 2010), which in turn enhances surface sensible heat fluxes (Bartusek et al. 2022), further elevating surface temperatures (Trenberth and Shea 2005). All these mechanisms contribute to the direct physical relationship between high pressure and temperature and precipitation extremes, enhancing compound hot and dry events.

Our findings are in line with previous studies where atmospheric patterns are identified as drivers behind spatially compound events (De Luca et al. 2020; Kornhuber et al. 2020; Ye and Messori 2020; Tian et al. 2024), as we show in the case of European regions (Figs. 7, 8, 9 and Figures S7-11). In addition, we quantify and locate the evolution of hot and dry compound synchronizations at the continental, regional and local scale, distinguishing between the boreal summer and winter seasons. This distinction is crucial, since the climatological features and the atmospheric patterns related to these two seasons are different, as also highlighted by our findings.

We find that, during summer, Great Britain, south Scandinavia, the Po valley, the Hungarian Plain and western Russia are the major hotspots for compound events (Fig. 3a), while the Mediterranean exhibits most of the significant increasing occurrences trends (Fig. 3c). This is partly reflected in the synchronizations detected in the JJA evolving network: Scandinavia and Great Britain are indeed affected by a large link density (Fig. 4a, NEU) and a high average degree centrality (Fig. 5a); in terms of synchronizations trends, a positive degree centrality trend is detected for England, Scandinavia and the Baltic states (Fig. 6a), albeit neither strong nor significant in most cases. In the Mediterranean, the East shows a DC increase and the West a slightly decrease (Fig. 6a).

NEU and WCE are the regions more strongly connected, with a high and increasing cross–regional link density, especially in the second half of the analysed period (Fig. 4c). To corroborate the strengthened NEU and WCE linkage in summer in 1991–2020, we find that the geopotential height anomaly corresponding to HCD in these two regions gets stronger in recent times over Europe by approximately 25–30 m (Fig. 7b,g and l,q). This is associated to temperature and precipitation extreme conditions: during HCD in 1991–2020, the frequency of temperature and precipitation extremes increases from 5% to 17% in NEU (more than a 3-fold increase) and from 5% to 13% in WCE (more than a 2-fold increase, see Fig. 9 and S9). Geopotential height composites reveal dynamical changes, with higher pressure in the North Atlantic and lower pressure over Greenland (Fig. 7b,g and l,q). This tendency resembles the positive phase of the summer North Atlantic Oscillation (Folland et al. 2009) (SNAO+), which is associated with summer climate variability over Europe and, in particular, with warm and dry conditions over the UK and Scandinavia (Folland et al. 2009; Linderholm et al. 2009). SNAO+ was one of the major drivers behind the 2018 European summer heatwave (Rousi et al. 2023). Several studies (Folland et al. 2009; Bladé et al. 2012; Rousi et al. 2021) agree on the increase of SNAO+ during the recent past, which would explain the stronger pressure anomaly we observe in Fig. 7g compared to Fig. 7b, leading to more compound synchronization between NEU and WCE (Fig. 7e,j and o,t). The increase in SNAO+ could be also the reason behind the relatively low number of connections between NEU and the Mediterranean (Fig. 7e), which decreases even more in the last 30 years (Fig. 7j), especially in the case of WMed and the Balkans. SNAO+ is in fact associated with wet conditions in southern Europe, especially in the Eastern Mediterranean region (Mariotti and Arkin 2007; Folland et al. 2009; Linderholm et al. 2009), and this relation is expected to increase (Bladé et al. 2012). By comparing the composites in Fig. 7a–b with the respective ones in Fig. 7f–g, we notice that the negative pressure anomaly over the Mediterranean becomes stronger (decreasing by approximately 20–25 m) and more significant in recent times. As for the atmospheric conditions related to WCE events in JJA (Fig. 7k,p), we still observe lower pressure over Greenland and higher pressure over northern Europe in the last 30 years, which could still indicate a stronger SNAO+ condition. However, we do not observe a clear temporal trend in SNAO daily index between 1941–1970 and 1991–2020 (Fig. 10b), and yet we do find it to be more intense during NEU high compound days both in 1941–1970 and 1991–2020 (Fig. 10d). Regarding the Mediterranean, thermodynamical effects and local land-atmosphere feedback could be more important to explain hot and dry extremes and their trends compared to northwestern Europe (Suarez-Gutierrez et al. 2020; Rousi et al. 2022).

During winter, the Mediterranean appears to be the most affected region by hot and dry events (Fig. 3b). The regional link density is higher in southern and central Europe (Fig. 4b) as well as the DC (Fig. 5b), especially in the West. Moreover, EMed and many nodes in WCE are dominated by an increasing DC (Fig. 6b), although few of these locations display a compound increase (Fig. 3d). NEU appears to be the only region with a clear decrease

of significant synchronizations: its regional link density declines (Fig. 4b) together with the NEU–WCE cross-regional link density (Fig. 4d). A low and decreasing DC is detected in NEU, except for Great Britain, where, although decreasing, the DC appears high on average (Figs. 5b and 6b).

By looking at the atmospheric conditions related to compound events during DJF in the Mediterranean, we notice that the increase of EMed and WMed spatial synchronizations (Fig. 8e,j and o,t) comes along with a lower pressure in northern Europe and North Atlantic and a higher pressure over central southern Europe and tropical North Atlantic, with a more pronounced low-high north–south dipole located over Europe (Fig. 8a–d, f–i and k–n, p–s). This pattern could be related to winter NAO, and in particular to its positive phase. NAO+ is associated with lower winter precipitation and higher temperatures over the Mediterranean (Rousi et al. 2020) and it is also expected to have a positive trend (Rousi et al. 2020, 2017, 2021; Linderholm et al. 2009). Moreover, since NAO+ has an opposite effect over northern latitudes, causing higher than usual precipitation (Rousi et al. 2020), it could explain the few detected compound synchronizations between NEU and the south, and the associated negative trends (Figs. 4d, 6b and f). We do find a positive trend of NAO intensity during 1991–2020 compared to 1941–1970, as shown in Fig. 10a. We also show that, during 1991–2020 HCD in WMed and EMed, NAO+ conditions are more frequent (Figs. 10c and S12c). This is also confirmed by the higher number of Mediterranean HCD in 1991–2020 during months with stronger NAO (Figure S13).

Several atmospheric variability patterns could potentially influence wintertime climate in Europe together with NAO. For instance, Madonna et al. (2021) explore in details the association and the impacts of NAO, blocking and jet streams over Europe, showing that these could be coupled to amplify hot and dry conditions at the surface or, conversely, cause opposite effects. In their study, Mellado-Cano et al. (2019) explore the interactions between east Atlantic (EA) pattern and NAO and their impacts on Europe climate variability. They show that the simultaneous occurrence of EA and NAO positive phases in winter significantly correlates with higher than average temperatures over most of central and southern Europe, low precipitation over most of the Mediterranean and high precipitation over the British Isles and Scandinavia. This is in line with our findings and it demonstrates that the interplay among different atmospheric patterns is relevant for extremes occurrences.

Climate change and its impacts on atmosphere dynamics could potentially foster the simultaneous occurrences of hot and dry extremes at different locations. As previously discussed, the NAO plays a key role in shaping weather and climate conditions in Europe. Its changes in amplitude and location may result from human induced climate change (Rousi et al. 2020). The weakening of the Atlantic meridional overturning circulation could also cause the increase of compound events, by triggering extreme heatwaves over central Europe in summer and enhanced storm track activity toward northwestern Europe in winter (Rousi et al. 2021). Another important mechanisms to take into account is the persistence of double jet streams over Europe, which Rousi et al. (2022) found to have an upward trend responsible for the accelerated heatwave increase in western Europe. Finally, Artic amplification (the accelerated warming of the Artic) is connected to persistent weather patterns in mid-latitudes, which lead to an increased probability of extreme weather events (Francis and Vavrus 2012), both during boreal winter (Cohen et al. 2020) and summer, when it could cause persistent hot-dry extremes (Coumou et al. 2018).

All these examples show how intricate the relations between different atmospheric patterns may be, but they also demonstrate the clear connection between global warming, atmosphere dynamics and weather extremes in Europe. We further expand these observations, linking them to the consequent rise of SCHADE events synchronizations. Our approach allow us to identify and quantify the synchronizations of these extremes for different regions in Europe and seasons. The evolving network framework is key to analyze the temporal and spatial variations of hot and dry extremes concurrences and locate them to the continental, regional and local scale.

5 Conclusions

In this study, we explore the evolution of spatially compound hot and dry extremes in Europe for boreal summer (JJA) and winter (DJF) during the period 1941–2020 in ERA5, using concepts and methods derived from network theory. Our results show that the distributions of compound extremes and their synchronizations strongly vary between the two seasons and European regions as well. We reveal that the increase of compounds frequency and synchronizations do not always coincide. For some locations the spatial concurrences are growing although compounds frequency is not significantly rising, as in the case of south-eastern Europe during winter and in some locations in Finland, north of Poland and the Baltic states in summer.

This work highlights spatio-temporal features of compound hot and dry extremes, focusing of the co-occurrences of these events at different locations. This is crucial to distinguish the effects of climate change on the spatial relationships among these events more than on the extremes themselves, and to understand more about compounds dynamics, given their intrinsically higher risk due to the combinations of the impacts. We apply our framework to hot

and dry events in Europe and analyze their characteristics, but the same approach could be employed for other types of compound weather and climate events.

This analysis could be further expanded by explicitly considering the intensity and duration of extremes, to check how these impact the spatio-temporal structure of synchronizations. Moreover, our approach could be applied to future climate projections, to assess if and how compounds features are going to change under different Shared Socioeconomic Pathways for specific regions. This would not only improve our understanding of these phenomena, but potentially support in extreme events predictions, improving forecasting schemes and adaptation strategies at key locations.

Supplementary Information The online version contains supplementary material available at https://doi.org/10.1007/s00382-025-07626-7.

Author Contributions All authors contributed to the study conception and design. Material preparation, data collection and analysis were performed by Domenico Giaquinto. The first draft of the manuscript was written by Domenico Giaquinto and all authors commented on previous versions of the manuscript. All authors read and approved the final manuscript.

Funding Open access funding provided by Università degli Studi di Napoli Federico II within the CRUI-CARE Agreement. The research leading to these results has received funding from the HORIZON-RIA project PREVENT (grant no. 101081276) and from the German Federal Ministry of Education and Research (BMBF) through the ClimXtreme project Phase 2 (subproject PERSEVERE, grant 01LP2322D) (Giorgia Di Capua).

Data Availability The data that supports the findings of this study are publicly available online: ERA5 datasets are publicly available on the Copernicus website (Copernicus Climate Change Service, Climate Data Store, 2019).

Declarations

Conflict of interest The authors have no relevant financial or non-financial interests to disclose.

References

Agarwal A, Caesar L, Marwan N, Maheswaran R, Merz B, Kurths J (2017) Multi-scale event synchronization analysis for unravelling climate processes: a wavelet-based approach. Nonlinear Process Geophys 24:599–611. https://doi.org/10.5194/npg-24-599-2017

AghaKouchak A, Chiang F, Huning LS, Love CA, Mallakpour I, Mazdiyasni O, Moftakhari H, Papalexiou SM, Ragno E, Sadegh M (2020) Climate extremes and compound hazards in a warming world. Annu Rev Earth Planet Sci 48:519–548. https://doi.org/10.1146/annurev-earth-071719-055228

Arianos S, Bompard E, Carbone A, Xue F (2009) Power grid vulnerability: a complex network approach. Chaos An Interdiscip J Nonlinear Sci. https://doi.org/10.1063/1.3077229

Ausloos M, Petroni F, Johnson J, Zhang Y-C, Rotundo G (2017) How visas shape and make visible the geopolitical architecture of the planet. Physica A 484:267–275. https://doi.org/10.1016/j.physa.2017.05.003

Ballester J, Quijal-Zamorano M, Méndez Turrubiates RF, Pegenaute F, Herrmann FR, Robine JM, Basagaña X, Tonne C, Antó JM, Achebak H (2023) Heat-related mortality in Europe during the summer of 2022. Nat Med 29:1857–1866. https://doi.org/10.1038/s41591-023-02419-z

Bardoscia M, Livan G, Marsili M, Castaldi P, Battiston S (2021) The physics of financial networks. Nature Rev Phys 3:490–507. https://doi.org/10.1038/s42254-021-00322-5

Bartusek S, Kornhuber K, Ting M (2022) 2021 North American heatwave amplified by climate change-driven nonlinear interactions. Nat Clim Chang 12:1143–1150. https://doi.org/10.1038/s41558-022-01520-4

Benjamini Y, Hochberg Y (1995) Controlling the false discovery rate: a practical and powerful approach to multiple testing. J Roy Stat Soc: Ser B (Methodol) 57:289–300. https://doi.org/10.1111/j.2517-6161.1995.tb02031.x

Benjamini Y, Yekutieli D (2001) The control of the false discovery rate in multiple testing under dependency. Ann Stat. https://doi.org/10.1214/aos/1013699998

Berg A, Lintner BR, Findell K, Seneviratne SI, van Den Hurk B, Ducharne A, Chéruy F, Hagemann S, Lawrence DM, Malyshev S et al (2015) Interannual coupling between summertime surface temperature and precipitation over land: Processes and implications for climate change. J Clim 28:1308–1328. https://doi.org/10.1175/JCLI-D-14-00324.1

Bevacqua E, Maraun D, Vousdoukas M, Voukouvalas E, Vrac M, Mentaschi L, Widmann M (2019) Higher probability of compound flooding from precipitation and storm surge in Europe under anthropogenic climate change. Sci Adv. https://doi.org/10.1126/sciadv.aaw5531

Bladé I, Liebmann B, Fortuny D, van Oldenborgh GJ (2012) Observed and simulated impacts of the summer NAO in Europe: implications for projected drying in the Mediterranean region. Clim Dyn 39:709–727. https://doi.org/10.1007/s00382-011-1195-x

Boccaletti S, Latora V, Moreno Y, Chavez M, Hwang D-U (2006) Complex networks: structure and dynamics. Phys Rep 424:175–308. https://doi.org/10.1016/j.physrep.2005.10.009

Boers N, Bookhagen B, Marwan N, Kurths J, Ballesteros-Canovas JA (2013) Complex networks identify spatial patterns of extreme rainfall events of the South American Monsoon System. Geophys Res Lett 40:4386–4392. https://doi.org/10.1002/grl.50681

Boers N, Rheinwalt A, Bookhagen B, Barbosa HM, Marwan N, Trauth MH, Kurths J (2019) Complex networks reveal global pattern of extreme-rainfall teleconnections. Nature 566:373–377. https://doi.org/10.1038/s41586-018-0872-x

Bühlmann P (1997) Sieve bootstrap for time series, Bernoulli, pp. 123–148

Ciais P, Reichstein M, Viovy N, Granier A, Ogée J, Allard V, Aubinet M, Buchmann N, Bernhofer C, Carrara A et al (2005) Europe-wide reduction in primary productivity caused by the heat and

drought in 2003. Nature 437:529–533. https://doi.org/10.1038/nature03972
Cohen J, Zhang X, Francis J, Jung T, Kwok R, Overland J, Ballinger T, Bhatt U, Chen H, Coumou D et al (2020) Divergent consensuses on Arctic amplification influence on midlatitude severe winter weather. Nat Clim Chang 10:20–29. https://doi.org/10.1038/s41558-019-0662-y
Copernicus Climate Change Service (2024a) ESOTC 2023, Precipitation, https://climate.copernicus.eu/esotc/2023/precipitation, Accessed 11 Nov 2024
Copernicus Climate Change Service (2024b) European State of the Climate 2023, https://climate.copernicus.eu/esotc/2023, accessed: 11th November 2024
Copernicus Climate Change Service: Copernicus (2024c) 2023 is the hottest year on record, with global temperatures close to the 1.5°C limit, https://climate.copernicus.eu/copernicus-2023-hottest-year-record, Accessed 11 Nov 2024
Copernicus Climate Change Service (2024d) ESOTC 2023, River flow, https://climate.copernicus.eu/esotc/2023/river-flow, Accessed 11th Nov 2024
Copernicus Climate Change Service (2024e) ESOTC 2023, Soil moisture, https://climate.copernicus.eu/esotc/2023/soil-moisture, Accessed 11th Nov 2024
Copernicus Climate Change Service (2024f) Surface air temperature for June 2024, https://climate.copernicus.eu/surface-air-temperature-june-2024, Accessed 11th Nov 2024
Copernicus Climate Change Service (2024g) Precipitation, relative humidity and soil moisture for August 2023, https://climate.copernicus.eu/precipitation-relative-humidity-and-soil-moisture-august-2023, Accessed 11th Nov 2024
Coumou D, Petoukhov V, Rahmstorf S, Petri S, Schellnhuber HJ (2014) Quasi-resonant circulation regimes and hemispheric synchronization of extreme weather in boreal summer. In: Proceedings of the national academy of sciences, 111, 12 331–12 336, https://doi.org/10.1073/pnas.1412797111
Coumou D, Di Capua G, Vavrus S, Wang L, Wang S (2018) The influence of Arctic amplification on mid-latitude summer circulation. Nat Commun 9:2959. https://doi.org/10.1038/s41467-018-05256-8
De Luca P, Donat MG (2023) Projected changes in hot, dry, and compound hot-dry extremes over global land regions. Geophys Res Lett. https://doi.org/10.1029/2022GL102493
De Luca P, Messori G, Faranda D, Ward PJ, Coumou D (2020) Concurrent wet and dry hydrological extremes at the global scale. Earth Syst Dyn 11:251–266. https://doi.org/10.5194/esd-11-251-2020
Di Capua G, Kretschmer M, Runge J, Arias PA, Coumou D (2020) Tropical and mid-latitude teleconnections interacting with the Indian summer monsoon rainfall: a theory-guided causal effect network approach. Earth Syst Dyn 11:17–34. https://doi.org/10.5194/esd-11-17-2020
Di Capua G, Kretschmer M, Zappa G, Coumou D (2021) Drivers behind the summer 2010 wave train leading to Russian heatwave and Pakistan flooding. Npj Clim Atmosph Sci. https://doi.org/10.1038/s41612-021-00211-9
Di Napoli C, Pappenberger F, Cloke HL (2018) Assessing heat-related health risk in Europe via the Universal Thermal Climate Index (UTCI). Int J Biometeorol 62:1155–1165. https://doi.org/10.1007/s00484-018-1518-2
Donges JF, Schultz HC, Marwan N, Zou Y, Kurths J (2009) The backbone of the climate network. Europhys Lett. https://doi.org/10.1209/0295-5075/87/48007
Donges JF, Zou Y, Marwan N, Kurths J (2009) Complex networks in climate dynamics: comparing linear and nonlinear network construction methods. Eur Phys J Spec Topics 174:157–179. https://doi.org/10.1140/epjst/e2009-01098-2
Douris J, Kim G (2021) The atlas of mortality and economic losses from weather, climate and water extremes (1970-2019), WMO
Fan J, Meng J, Ashkenazy Y, Bunde A, Havlin S, Ludescher J, Schellnhuber HJ (2021) Statistical physics approaches to the complex Earth system. Phys Rep 896:1–84. https://doi.org/10.1016/j.physrep.2020.09.005
Fink AH, Brücher T, Krüger A, Leckebusch GC, Pinto JG, Ulbrich U (2004) The 2003 European summer heatwaves and drought-synoptic diagnosis and impacts. Weather 59:209–216. https://doi.org/10.1256/wea.73.04
Fischer E, Sippel S, Knutti R (2021) Increasing probability of record-shattering climate extremes. Nat Clim Chang 11:689–695. https://doi.org/10.1038/s41558-021-01092-9
Folland CK, Knight J, Linderholm HW, Fereday D, Ineson S, Hurrell JW (2009) The summer North Atlantic Oscillation: past, present, and future. J Clim 22:1082–1103. https://doi.org/10.1175/2008JCLI2459.1
Francis JA, Vavrus SJ (2012) Evidence linking Arctic amplification to extreme weather in mid-latitudes. Geophys Res Lett. https://doi.org/10.1029/2012GL051000
Giaquinto D, Marzocchi W, Kurths J (2023) Exploring meteorological droughts' spatial patterns across Europe through complex network theory, Nonlinear Processes in Geophysics Discussions, pp. 1–19, https://doi.org/10.5194/npg-30-167-2023
Goh K-I, Cusick ME, Valle D, Childs B, Vidal M, Barabási A-L (2007) The human disease network. Proc Natl Acad Sci 104:8685–8690. https://doi.org/10.1073/pnas.0701361104
Gudmundsson L, Rego FC, Rocha M, Seneviratne SI (2014) Predicting above normal wildfire activity in southern Europe as a function of meteorological drought. Environ Res Lett. https://doi.org/10.1088/1748-9326/9/8/084008
Gupta S, Shivam Sundaram K, Choudhury A, Roy S (2021) Complex network approach for detecting tropical cyclones. Clim Dyn 57:3355–3364. https://doi.org/10.1007/s00382-021-05871-0
Ha K-J, Seo Y-W, Yeo J-H, Timmermann A, Chung E-S, Franzke CL, Chan JC, Yeh S-W, Ting M (2022) Dynamics and characteristics of dry and moist heatwaves over East Asia. Npj Clim Atmos Sci 5:49. https://doi.org/10.1038/s41612-022-00272-4
Habibullah MS, Din BH, Tan S-H, Zahid H (2022) Impact of climate change on biodiversity loss: global evidence. Environ Sci Pollut Res 29:1073–1086. https://doi.org/10.1007/s11356-021-15702-8
Hall A, Qu X (2006) Using the current seasonal cycle to constrain snow albedo feedback in future climate change. Geophys Res Lett. https://doi.org/10.1029/2005GL025127
Hersbach H, Bell B, Berrisford P, Biavati G, Horányi A, Muñoz Sabater J, Nicolas J, Peubey C, Radu R, Rozum I, Schepers D, Simmons A, Soci C, Dee D (2023) ERA5 hourly data on single levels from 1940 to present, Copernicus Climate Change Service (C3S) Climate Data Store (CDS), https://doi.org/10.24381/cds.e2161bac
Ionita M, Tallaksen LM, Kingston DG, Stagge JH, Laaha G, Van Lanen HA (2017) The European 2015 drought from a climatological perspective. Hydrol Earth Syst Sci 21:1397–1419. https://doi.org/10.5194/hess-21-1397-2017
Ionita M, Caldarescu DE, Nagavciuc V (2021) Compound Hot and Dry Events in Europe: variability and Large-Scale Drivers. Front Clim 3:1–19. https://doi.org/10.3389/fclim.2021.688991
Iturbide M, Gutiérrez JM, Alves L, Bedia J, Cimadevilla E, Cofiño AS, Cerezo-Mota R, Fioreze C, García-Díez M, Herrera S et al (2020) An update of IPCC climate reference regions for subcontinental analysis of climate model data: definition and aggregated datasets. Earth Syst Sci Data. https://doi.org/10.5194/essd-12-2959-2020
Kautz L-A, Martius O, Pfahl S, Pinto JG, Ramos AM, Sousa PM, Woollings T (2022) Atmospheric blocking and weather extremes over the Euro-Atlantic sector - a review. Weather Clim Dyn 3:305–336. https://doi.org/10.5194/wcd-3-305-2022

Kornhuber K, Osprey S, Coumou D, Petri S, Petoukhov V (2019) Extreme weather events in early summer 2018 connected by a recurrent hemispheric wave-7 pattern. Environ Res Lett. https://doi.org/10.1088/1748-9326/ab13bf

Kornhuber K, Coumou D, Vogel E, Lesk C, Donges JF, Murray-Tortarolo G, Rockström J (2020) Amplified Rossby waves enhance risk of concurrent heatwaves in major breadbasket regions. Nat Clim Chang 10:48–53. https://doi.org/10.1038/s41558-019-0637-z

Kreiss J-P (1997) Asymptotical properties of residual bootstrap for autoregressions, Tech. Rep., Institute für Mathematik, Techn. Univ

Leeding R, Riboldi J, Messori G (2023) On Pan-Atlantic cold, wet and windy compound extremes. Weather Clim Extremes 39(100):524. https://doi.org/10.1016/j.wace.2022.100524

Lesk C, Coffel E, Winter J, Ray D, Zscheischler J, Seneviratne SI, Horton R (2021) Stronger temperature-moisture couplings exacerbate the impact of climate warming on global crop yields. Nature food 2:683–691. https://doi.org/10.1038/s43016-021-00341-6

Li D, Yuan J, Kopp RE (2020) Escalating global exposure to compound heat-humidity extremes with warming. Environ Res Lett. https://doi.org/10.1088/1748-9326/ab7d04

Linderholm HW, Folland CK, Walther A (2009) A multicentury perspective on the summer North Atlantic Oscillation (SNAO) and drought in the eastern Atlantic Region. J Quat Sci Publ Quat Res Assoc 24:415–425. https://doi.org/10.1002/jqs.1261

Lorenz R, Argüeso D, Donat MG, Pitman AJ, van den Hurk B, Berg A, Lawrence DM, Chéruy F, Ducharne A, Hagemann S et al (2016) Influence of land-atmosphere feedbacks on temperature and precipitation extremes in the GLACE-CMIP5 ensemble. J Geophys Res Atmosph 121:607–623. https://doi.org/10.1002/2015JD024053

Ludescher J, Bunde A, Franzke C, Schellnhuber HJ (2021) Network-based forecasting of climate phenomena. Proc Natl Acad Sci. https://doi.org/10.1073/pnas.1922872118

Madonna E, Pasquier JT, Croci-Maspoli M, Weigel AP, Raible CC (2021) Reconstructing winter climate anomalies in the Euro-Atlantic sector using circulation patterns. Weather Clim Dyn 2:777–794. https://doi.org/10.5194/wcd-2-777-2021

Malik N, Marwan N, Kurths J (2010) Spatial structures and directionalities in Monsoonal precipitation over South Asia. Nonlinear Process Geophys 17:371–381. https://doi.org/10.5194/npg-17-371-2010

Malik N, Bookhagen B, Marwan N, Kurths J (2012) Analysis of spatial and temporal extreme monsoonal rainfall over South Asia using complex networks. Clim Dyn 39:971–987. https://doi.org/10.1007/s00382-011-1156-4

Manning C, Widmann M, Bevacqua E, Van Loon AF, Maraun D, Vrac M (2018) Soil moisture drought in Europe: a compound event of precipitation and potential evapotranspiration on multiple time scales. J Hydrometeorol 19:1255–1271. https://doi.org/10.1175/JHM-D-18-0017.1

Manning C, Widmann M, Bevacqua E, Van Loon AF, Maraun D (2019) Increased probability of compound long-duration dry and hot events in Europe during summer (1950–2013). Environ Res Lett. https://doi.org/10.1088/1748-9326/ab23bf

Mariotti A, Arkin P (2007) The North Atlantic Oscillation and oceanic precipitation variability. Clim Dyn 28:35–51. https://doi.org/10.1007/s00382-006-0170-4

Maslov S, Sneppen K, Zaliznyak A (2004) Detection of topological patterns in complex networks: correlation profile of the internet. Physica A 333:529–540. https://doi.org/10.1016/j.physa.2003.06.002

Mellado-Cano J, Ortega P, Martín-Chivelet J, Díaz JJ, Jiménez M, Montoya M, Gómez-Pellicer A, Moreno A (2019) Examining the North Atlantic Oscillation, East Atlantic pattern, and jet variability since 1685. J Clim 32:6285–6298. https://doi.org/10.1175/JCLI-D-19-0135.1

Mitchell D, Kornhuber K, Wolff J, Huntingford C (2019) The day the 2003 European heatwave record was broken. Lancet Planetary Health 3:e290–e292. https://doi.org/10.1016/S2542-5196(19)30106-8

Noguchi K, Gel YR, Duguay CR (2011) Bootstrap-based tests for trends in hydrological time series, with application to ice phenology data. J Hydrol 410:150–161. https://doi.org/10.1016/j.jhydrol.2011.09.008

Peel MC, Finlayson BL, McMahon TA (2007) Updated world map of the Köppen-Geiger climate classification. Hydrol Earth Syst Sci 11:1633–1644. https://doi.org/10.5194/hess-11-1633-2007

Perkins SE, Alexander LV (2013) On the measurement of heat waves. J Clim 26:4500–4517. https://doi.org/10.1175/JCLI-D-12-00383.1

Quian Quiroga R, Kreuz T, Grassberger P (2002) Event synchronization: a simple and fast method to measure synchronicity and time delay patterns. Phys Rev E. https://doi.org/10.1103/PhysRevE.66.041904

Rheinwalt A, Marwan N, Kurths J, Werner P (2012) Boundary effects in network measures of spatially embedded networks. In: 2012 SC Companion: high performance computing, networking storage and analysis, pp 1082–1103, IEEE, https://doi.org/10.1209/0295-5075/100/28002

Rheinwalt A, Marwan N, Kurths J, Werner P (2016) Non-linear time series analysis of precipitation events using regional climate networks for Germany. Clim Dyn 46:1065–1074. https://doi.org/10.1007/s00382-015-2632-z

Robine J-M, Cheung SLK, Le Roy S, Van Oyen H, Griffiths C, Michel J-P, Herrmann FR (2008) Death toll exceeded 70,000 in Europe during the summer of 2003. CR Biol 331:171–178. https://doi.org/10.1016/j.crvi.2007.12.001

Rousi E, Anagnostopoulos C, Tolika K, Maheras P (2017) An NAO climatology in reanalysis data with the use of self-organizing maps, In: Perspectives on atmospheric sciences, pp 853–859, Springer International Publishing, https://doi.org/10.1007/978-3-319-35095-0_103

Rousi E, Anagnostopoulos C, Fragkidis S, Hegerl GC, Paschalidou AK (2020) Implications of winter NAO flavors on present and future European climate. Climate 8:13. https://doi.org/10.3390/cli8010013

Rousi E, Anagnostopoulos C, Fragkidis S, Hegerl GC, Paschalidou AK (2021) Changes in North Atlantic atmospheric circulation in a warmer climate favor winter flooding and summer drought over Europe. J Clim 34:2277–2295. https://doi.org/10.1175/JCLI-D-20-0311.1

Rousi E, Kornhuber K, Beobide-Arsuaga G, Luo F, Coumou D (2022) Accelerated western European heatwave trends linked to more-persistent double jets over Eurasia. Nat Commun 13:3851. https://doi.org/10.1038/s41467-022-31432-y

Rousi E, Vautard R, Barbier C, Jézéquel A, Otto FEL, Keraunos Y, Haylock MR, Hegerl GC (2023) The extremely hot and dry 2018 summer in central and northern Europe from a multi-faceted weather and climate perspective. Nat Hazard 23:1699–1718. https://doi.org/10.5194/nhess-23-1699-2023

Ruffault J, Moron V, Trigo R, Curt T (2016) Objective identification of multiple large fire climatologies: an application to a Mediterranean ecosystem. Environ Res Lett. https://doi.org/10.1088/1748-9326/11/7/075006

Russo S, Sillmann J, Fischer EM (2015) Top ten European heatwaves since 1950 and their occurrence in the coming decades.

Environ Res Lett. https://doi.org/10.1088/1748-9326/10/12/124003
Seneviratne S, Nicholls N, Easterling D, Goodess C, Kanae S, Kossin J, Luo Y, Marengo J, McInnes K, Rahimi M et al (2012) Changes in climate extremes and their impacts on the natural physical environment, managing the risks of extreme events and disasters to advance climate change adaptation. A Special Report of Working Groups I and II of the Intergovernmental Panel on Climate Change (IPCC). https://doi.org/10.1017/CBO9781139177245.006
Seneviratne SI, Corti T, Davin EL, Hirschi M, Jaeger EB, Lehner I, Orlowsky B, Teuling AJ (2010) Investigating soil moisture-climate interactions in a changing climate: A review. Earth Sci Rev 99:125–161. https://doi.org/10.1016/j.earscirev.2010.02.004
Seneviratne SI, Wartenburger R, Guillod BP, Hirsch AL, Vogel MM, Brovkin V, van Vuuren DP, Schaller N, Boysen L, Calvin KV et al (2018) Climate extremes, land-climate feedbacks and land-use forcing at 15 C. Philos Trans R Soc A Math Phys Eng Sci. https://doi.org/10.1098/rsta.2016.0450
Seneviratne SI, Zhang X, Adnan M, Badi W, Dereczynski C, Luca AD, Ghosh S, Iskandar I, Kossin J, Lewis, S (2021) Weather and climate extreme events in a changing climate, Climate Change, et al. The physical science basis. Contribution of Working Group I to the Sixth Assessment Report of the Intergovernmental Panel on Climate Change 2021. https://doi.org/10.1017/9781009157896.013
Seo Y-W, Ha K-J (2022) Changes in land-atmosphere coupling increase compound drought and heatwaves over northern East Asia. Npj Clim Atmosph Sci. https://doi.org/10.1038/s41612-022-00325-8
Spinoni J, Naumann G, Vogt JV, Barbosa P (2014) World drought frequency, duration, and severity for 1951–2010. Int J Climatol 34:2792–2804. https://doi.org/10.1002/joc.3875
Spinoni J, Naumann G, Vogt J, Barbosa P (2015) European drought climatologies and trends based on a multi-indicator approach. Global Planet Change 127:50–57. https://doi.org/10.1016/j.gloplacha.2015.01.012
Spinoni J, Naumann G, Vogt JV, Barbosa P (2015) The biggest drought events in Europe from 1950 to 2012. J Hydrol Regional Stud 3:509–524. https://doi.org/10.1016/j.ejrh.2015.01.001
Spinoni J, Naumann G, Vogt JV (2017) Pan-European seasonal trends and recent changes of drought frequency and severity. Global Planet Change 148:113–130. https://doi.org/10.1016/j.gloplacha.2016.11.013
Stott PA, Stone DA, Allen MR (2004) Human contribution to the European heatwave of 2003. Nature 432:610–614. https://doi.org/10.1038/nature03089
Strnad FM, Boers N, Goswami B, Rheinwalt A, Bookhagen B, Barbosa HMJ, Kurths J (2023) Propagation pathways of Indo-Pacific rainfall extremes are modulated by Pacific sea surface temperatures. Nat Commun 14:5708. https://doi.org/10.1038/s41467-023-41400-9
Suarez-Gutierrez L, Li C, Cardoso-Bihlo E, Kadow C, Cubasch U (2020) Dynamical and thermodynamical drivers of variability in European summer heat extremes. Clim Dyn 54:4351–4366. https://doi.org/10.1007/s00382-020-05233-2
Sutanto SJ, Vitolo C, Di Napoli C, D'Andrea M, Van Lanen HA (2020) Heatwaves, droughts, and fires: Exploring compound and cascading dry hazards at the pan-European scale. Environ Int. https://doi.org/10.1016/j.envint.2019.105276
Tabari H, Willems P (2023) Global risk assessment of compound hot-dry events in the context of future climate change and socioeconomic factors. NPJ Clim Atmosph Sci 6:74. https://doi.org/10.1038/s41612-023-00401-7
Tavakol A, Rahmani V, Harrington J Jr (2020) Temporal and spatial variations in the frequency of compound hot, dry, and windy events in the central United States. Sci Rep. https://doi.org/10.1038/s41598-020-72624-0
Teuling AJ, Van Loon AF, Seneviratne SI, Lehner I, Aubinet M, Heinesch B, Bernhofer C, Grünwald T, Prasse H, Spank U (2013) Evapotranspiration amplifies European summer drought. Geophys Res Lett 40:2071–2075. https://doi.org/10.1002/grl.50495
Tian Y, Ghausi SA, Zhang Y, Zhang M, Xie D, Cao Y, Mei Y, Wang G, Zhong D, Kleidon A (2023) Radiation as the dominant cause of high-temperature extremes on the eastern Tibetan Plateau. Environ Res Lett. https://doi.org/10.1088/1748-9326/acd805
Tian Y, Giaquinto D, Di Capua G, Claassen JN, Ali J, Li H, De Michele C (2024) Historical changes in the Causal Effect Networks of compound hot and dry extremes in central Europe. Commun Earth Environ. https://doi.org/10.1038/s43247-024-01934-2
Trenberth KE, Shea DJ (2005) Relationships between precipitation and surface temperature. Geophys Res Lett. https://doi.org/10.1029/2005GL022760
Tripathy KP, Mishra AK (2023) How unusual is the 2022 European compound drought and heatwave event? Geophys Res Lett. https://doi.org/10.1029/2023GL105453
Tsonis AA, Roebber PJ (2004) The architecture of the climate network. Physica A 333:497–504
Vallejo-Bernal SM, Ramos AM, Pereira AR, Liberato ML, Trigo RM, Lavers DA (2023) The role of atmospheric rivers in the distribution of heavy precipitation events over North America. Hydrol Earth Syst Sci 27:2645–2660. https://doi.org/10.5194/hess-27-2645-2023
Vogel MM, Orth R, Cheruy F, Hagemann S, Lorenz R, van den Hurk BJ, Seneviratne SI (2017) Regional amplification of projected changes in extreme temperatures strongly controlled by soil moisture-temperature feedbacks. Geophys Res Lett 44:1511–1519. https://doi.org/10.1002/2016GL071235
White RH, Madonna E, Ulbrich U, Czaja A, Pinto JG (2022) From atmospheric waves to heatwaves: a waveguide perspective for understanding and predicting concurrent, persistent, and extreme extratropical weather. Bull Am Meteor Soc 103:E923–E935. https://doi.org/10.1175/BAMS-D-21-0170.1
Wilhite DA, Glantz MH (1985) Understanding: the drought phenomenon: the role of definitions. Water Int 10:111–120. https://doi.org/10.1080/02508068508686328
World Meteorological Organization (2017) WMO Guidelines on the calculation of Climate Normals (WMO-No. 1203), Tech. rep., WMO, Geneva, https://library.wmo.int/idurl/4/55797
Yadav N, Rajendra K, Awasthi A, Singh C, Bhushan B (2023) Systematic exploration of heat wave impact on mortality and urban heat island: A review from 2000 to 2022, Urban Climate, 51, 101 622, https://doi.org/10.1016/j.uclim.2023.101622
Ye K, Messori G (2020) Two leading modes of wintertime atmospheric circulation drive the recent warm Arctic-cold Eurasia temperature pattern. J Clim 33:5565–5587. https://doi.org/10.1175/JCLI-D-19-0403.1
Ying N, Zhou D, Han Z, Chen Q, Ye Q, Xue Z (2020) Rossby waves detection in the CO2 and temperature multilayer climate network, Geophysical Research Letters, 47, e2019GL086 507

Zhang X, Chen N, Sheng H, Ip C, Yang L, Chen Y, Sang Z, Tsegaye T, Lim P, Rajabifard A et al (2019) Urban drought challenge to 2030 Sustainable Development Goals. Sci Total Environ. https://doi.org/10.1016/j.scitotenv.2019.07.342

Zhao T, Connor TS, Hao X, Chen X, Wang F, Yin S (2024) Compound dry and hot events over major river basins of the world from 1921 to 2020. Weather Clim Extrem. https://doi.org/10.1016/j.wace.2024.100679

Zscheischler J, Orth R, Seneviratne SI (2017) Bivariate return periods of temperature and precipitation explain a large fraction of European crop yields. Biogeosciences 14:3309–3320. https://doi.org/10.5194/bg-14-3309-2017

Zscheischler J, Westra S, Van Den Hurk BJ, Seneviratne SI, Ward PJ, Pitman A, AghaKouchak A, Bresch DN, Leonard M, Wahl T et al (2018) Future climate risk from compound events. Nat Clim Chang 8:469–477. https://doi.org/10.1038/s41558-018-0156-3

Zscheischler J, Martius O, Westra S, Bevacqua E, Raymond C, Horton RM, van den Hurk B, AghaKouchak A, Jézéquel A, Mahecha MD et al (2020) A typology of compound weather and climate events. Nature Rev Earth Environ 1:333–347. https://doi.org/10.1038/s43017-020-0060-z